Fabrication and Characterization of Nanoscale Elements of a Miniaturized Gas Ionization Sensor

Nika Azmoodeh

A Thesis

in

The Department

of

Electrical and Computer Engineering

Presented in Partial Fulfillment of Requirements

For the Degree of Master of Applied Science (Electrical Engineering) at

Concordia University

Montreal, Quebec, Canada

August 2008

Your file Votre référence
ISBN: 978-0-494-45480-0
Our file Notre référence
ISBN: 978-0-494-45480-0

ABSTRACT

Study, Fabrication and Characterization of Nanoscale Elements of a Miniaturized Gas Ionization Sensor

Nika Azmoodeh

In this thesis the nanoscale elements of a Gas Ionization Sensor (GIS) were studied, designed and fabricated. A GIS is working by fingerprinting the ionization breakdown voltage of unknown gases which displays good selectivity even in the very low gas pressure. In GIS, electron impact ionization mechanism leads to the breakdown of gas inside an ionization cell . Since breakdown voltage (V_b) is a unique quantity of each gas, by measuring this voltage, the existence and type of the unknown gases can be found. To fabricate the GIS, vertically aligned arrays of AgNWs were employed. The AgNWs were synthesized by template-assisted electroplating method. To obtain freestanding metals nanowires without any bundling, Anodized Alumina Oxide (AAO) template with well ordered pore morphology was required.

The AAO templates were fabricated using the modified two steps anodization process. By applying various anodization conditions, AAO templates with interpore distance varying from 40nm to 150nm were fabricated. Besides, the dependency of the interpore distance and applied voltage in the AAO was confirmed.

The freestanding AgNWs fabricated in the pores of AAO were then used as the cathode in the two parallel plate ionization cell to act as the field amplifier to decrease the field ionization threshold voltage.

The GIS was characterized and compared to its AuNWs counterparts. This new device exhibit improvement compared to its previous AuNWs GIS, as the breakdown voltages were further reduced. The reduction of V_b was attributed to the lower workfunction of silver compared to that of gold.

ACKNOWLEDGMENTS

I would like to express my sincere gratitude to my supervisor, Dr. Mojtaba Kahrizi for his great supervision, encouragement, and support during my study. His valuable guidance and assistance are highly appreciated.

I am greatly thankful to Dr. Simona Badilescu for her attention, kindness, and valuable scientific suggestion and assistance regarding my chemical experiments.

Special appreciation is due to my research colleague, Ramin Banan Sadeghian, whose assistance during this research is unforgettable.

I would also like to thank my other colleagues in the nanotechnology lab, Mitra Esfahani, Maryam Etezad, Svetlana Spitsina, and Farah Fida for their friendship and support.

I would also like to acknowledge the department of mining, metals and material engineering in McGill University for providing SEM and XRD facilities for this project.

I am also thankful to my supervisory committee for their insight reviews, critics, and invaluable feedback.

Most importantly I would like to express my sincere thanks to my dearest family. To my sister, Pegah, and my two brothers, Arash, and Barzin for their invaluable care and encouragement during these years. I am very much indebted to my dear parents, Mehran, and Ahmad, for all their supports, encouragements, and patience not only during this work, but also throughout my whole life.

TABLE OF CONTENTS

LIST OF FIGURES

LIST OF TABLES

LIST OF ACRONYMS

AAO	Anodized Aluminium Oxide
AC	Alternative Current
AFM	Atomic Force Microscopy
AgNWs	Silver Nanowires
AuNWs	Gold Nanowires
CNT	Carbon Nanotube
DC	Direct current
DI Water	De-Ionized water
ECD	Electron Capture Detector
FET	Field Effect Transistor
GIS	Gas Ionization Sensor
LED	Light Emitting Diode
NC Mode	Non-Contact mode
PAA	Porous Anodic Alumina
PID	Photo Ionization Detector
PS	Polystyrene
PSD	Position Sensitive Detector
RF	Radio Frequency
SEM	Scanning Electron Microscope

SMU	Source-Measure Unit
SPM	Scanning Probe Microscopy
STM	Scanning Tunnelling Microscopy
TEM	Tunnelling Electron Microscopy
TESP	Tapping Mode Etched Silicon Probe
VLS	Vapour Liquid Solid
XRD	X-Ray Diffraction
0-D	0 Dimension
1-D	1 Dimension
2-D	2 Dimension

LIST OF SYMBOLS

D_p	Pore diameter	[nm]
D_c	Interpore distance	[nm]
T_p	Height of the pore	[μm]
b	Thickness of the oxide	[μm]
r	Equilibrium pore base radius of curvature	[μm]
K	Spring Constant	[Nm^{-1}]
F	Force	[N]
x	cantilever deflection	[μm]
λ	Wavelength of the incident light	[m]
J	Current density	[Acm^{-2}]
e	Charge per electron	1.602×10^{-19}[C]
n_e, n_i	Concentration of electrons and ions	[cm^{-3}]
I	Current	[A]
L	Length of nanowires	[μm]
P_{AAO}	AAO porosity	–
p	Gas pressure	[torr]
N	Number of gas molecules	–
$\frac{dn}{dt}$	Rate of production of charged particles	[cm^{-3} s^{-1}]

V_b	Breakdown voltage	[V]
d, d_{gap}	Interelectrode distance	[cm]
E	Effective electric field	[Vcm^{-1}]
E_{app}	Applied electric field	[Vcm^{-1}]
E_{loc}	Local electric field at the sharp tip	[Vcm^{-1}]
α	Townsend's primary ionization coefficient	[cm-1]
γ	Secondary electron factor by ion bombardment	_
β	Electric field enhancement factor	_

Chapter 1: Introduction

1.1. Goal and motivation of this research

There is an ongoing research in our lab, to develop a novel miniature gas ionization sensor based on free-standing gold nanowires [1]. A typical gas ionization sensor (GIS) is operating by fingerprinting the ionization breakdown voltages of the gases to be identified [2] . The main advantages of the GIS comparing to the conventional catalyst based sensors is its high selectivity and sensivity. The GIS overcome the selectivity issue, by identifying the unique ionization characteristic of each single gas, where some other ionization sensors such as photo-ionization detectors (PIDs) or electron capture detectors (ECDs) are not appropriate to direct application for mixture of gases [2]. The GIS, as a sensor with very high sensivity, can also detect gases with low chemical adsorption energy such as inert gases, even at a very low gas pressure. To obtain these qualities, it is very important to grow free self-standing metallic nanowires.

The GIS fabricated in our lab was base on arrays of free standing gold nanowires, which were synthesized by a template-based method. One of the difficulties, encountering in growing gold nanowires with template-base electrochemical deposition was that when the wires grow more than few microns, they were started to bundle and collapse on each other. The main reason for this drawback was the high porosity of the commercial templates, and the random configuration of the pores. To solve this problem it was suggested [3] to reduce the porosity of the commercial template by applying polystyrene (PS) microspheres to block some random pores of the template.

According to the problematic situation of using the commercial template, we decided to work on homemade template in which to have full control over the pores morphology and configuration. Therefore, a considerable part of this thesis is contributed to the theory of the Anodized Aluminum Oxide (AAO) template, and synthesizing process. The affecting parameters on the morphology of AAO were studied and AAO template with different pore diameter and interpore distance were fabricated [4].

As it is known, measuring of a gas breakdown voltage is a tool to identify any unknown gases in the GIS. Since, the work function of the metallic nanowire has a significant effect on the breakdown voltage of the gases [3], we have examined the other noble metals in fabrication of the GIS, such as silver and silver-gold alloy. Therefore, the other division of this thesis is contributed to the fabrication of self-standing silver and silver-gold alloy nanowire, fabrication of the GIS base on these nanowires, and characterization of the fabricated GIS.

1.2. Organization of the thesis

This thesis is organized as follow:

► *Chapter 2* presents an overview and background of different techniques in growing nanowires and the advantage of the template base technique. This chapter also provides a review of the structure and composition of AAO template and theory of AAO fabrication.

► *Chapter 3* gives a brief overview of characterization and measurement techniques used for this research. The theory of the Atomic Force Microscopy (AFM), Scanning Electron Microscope (SEM) and X-Ray Diffraction (XRD) were explained in this chapter.

► *Chapter 4* describes the AAO template fabrication process in detail. The results and discussion regarding the AAO templates were also provided in this chapter.

► *Chapter 5* presents the synthesis process of metallic nanowires and the characterization of the self-standing metallic nanowires. Besides, fabrication of GIS made of silver nanowires and the device characterization and comparison with the GIS made of gold nanowires is described in this chapter.

► *Chapter 6* gives the conclusion and contribution of this research.

Chapter 2: Background and review

2.1. Overview

The terms miniaturization or simply down-sizing the existing microstructures into nano scale regimes has been attracted increasing attention in all technologies as they might supply a large number of opportunities for modern science and technology [5].

As an example the terms "smaller" in microelectronics and integrated circuits can be interpreted as more components per chip, faster processing time, lower cost, and less power consumption. So, in last few decades it has been lots of emphasis on the fabrication of nanostructures and finding their application in electronic and boielectronic devices.

Nanostructures are defined as structure which have at least one dimension between1-100 nm and can generally divided into 0-Dimention (0D) nanostructures or quantum dots, 1-dimention (1D) nanostructures, and 2-Dimentional (2D) nanostructures or quantum wells [6, 7].

Among all these nanostructures, one-dimensional (1D) ones like wires, rods, belts and tubes are believed to provide good opportunity of applications in mesoscopic physics and also they play important role as interconnect in upcoming generations of nanometre-scale electronics, optoelectronic, and electromechanical devices [6].

Basically, Nanowires in accordance with material used in their building block can be divided into two main groups which include:

1. Metallic nanowires
2. Semiconducting nanowires

2.1.1. Metallic nanowires

Metallic nanowires are miniaturized wires which have received considerable attention due to its particular characteristics to utilize them as nano sensors. For instance, it has been observed recently [5] that the metallic nanowires are sensitive to the adsorption of a molecule onto them and therefore has the potential of being used as chemical sensors.

Besides, in this research metallic nanowires, due to their tiny features, were used as field-amplifiers to reduce the field ionization threshold voltages, and have the application in a novel gas ionization sensor.

In addition of sensor application, metallic nanowires have also the potential application as connectors and single-atom switches[8].

2.1.2. Semiconducting nanowires

Semiconducting nanowires can be predictably fabricated in single crystal form, by controlling all the morphology parameters such as doping and chemical composition. Semiconducting nanowires are being used as variety range of devices such as LEDs, bipolar junctions, p-n junctions, logic gates, and even computational circuits [9].

One of the other common and important applications of semiconducting nanowires is to fabricate field effect transistor (FET) with them. The FET will be supported in an oxidized silicon substrate with the base of silicon acting as a back gate to change the electrostatic potential of the nanowires. Therefore, source and drain electrodes will be made from the two metal contacts on either end of the nanowires [7] [10].

In addition, as the conductance of the field effect transistor (FET) can be modulated by applied voltage to silicon back gate, FETs with semiconductor nanowires are good candidates to synthesize chemical and biological sensors.

2.2. Fabrication of nanowires

Basically, there are two main approaches which are employed to synthesize nanowires namely top-down and bottom-up approaches.

The top-down, includes standard traditional micro fabrication such as lithography, etching and deposition where for the case of nanotechnology, nano-scale features will be pattern on bulk materials. Although these techniques are successful in many cases, but they normally become very complex and expensive when they are applied for nano-scale dimensions.

Contrary to the top down, the bottom-up employs the natural capability of molecules to be self-assembles from their single-molecule components into the desired nanostructures.

Figure 2.1 illustrates the changing of these two approaches by miniaturizing the size over the past few decades.

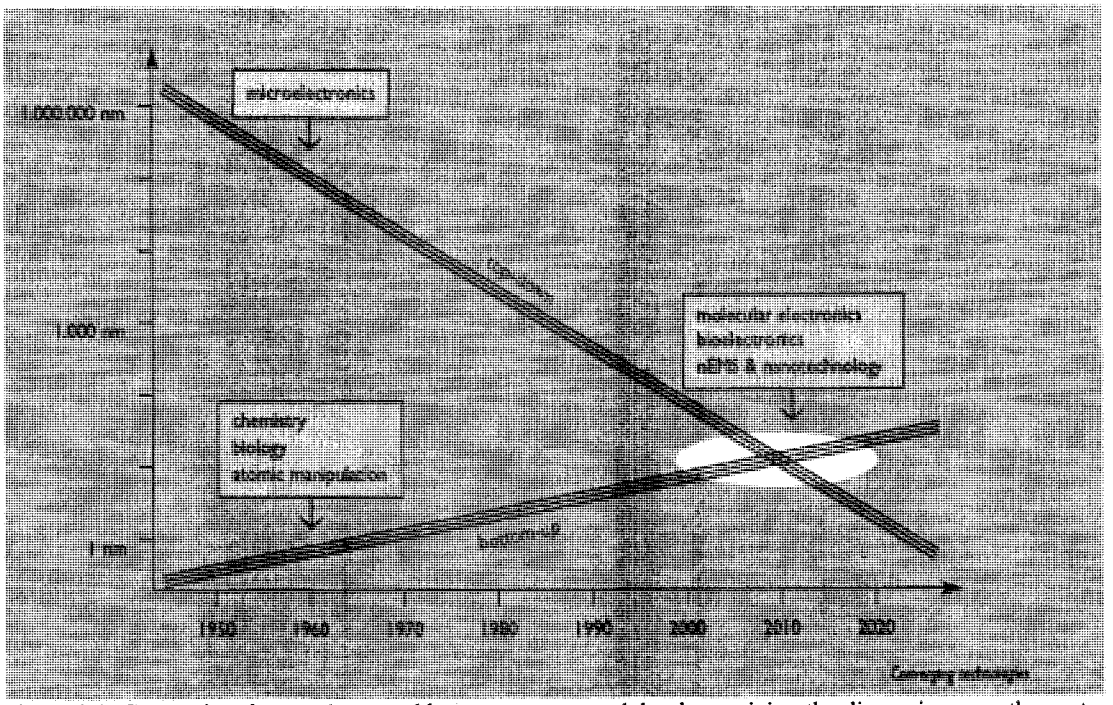

Figure 2.1. Comparing the top-down and bottom-up approach by down-sizing the dimension over the past few decades [11].

As it can be seen, by downsizing the dimension of the fabricated device over the past few decades, there is a promising rout to fabricate nanostructures via bottom-up approach. With the bottom-up approach smaller devices can be fabricated with lower cost than using the lithography. Besides, there will be less waste of material in compare with etching in top-down approach. But the main reason of the augmentation of bottom-up approach is that with this approach there will be more control over the morphology of the nanostructure where parallel nanostructure can be synthesized in a shorter time. In addition, this approach will enable scientists to fabricate complex patterns and structure by self assembly [12]. Among all the bottom-up techniques, templating is one the most economical techniques with the advantage of complete control over the size and

morphology of nanostructures. As this method was applied to fabricate metallic nanowires in this research, a background and review will be given regarding the template- assisted techniques in the following section.

2.2.1. Template–assisted techniques

Template-base fabrication of nanomaterials involves synthesising of desired nanostructures within the pores or channels of nanoporous membranes [13]. Since the pores within the templates are cylindrical with uniform diameter, variety of nano materials can be obtained within these pores.

Template–assisted technique is extremely general with regard to type of material that can be grown inside the pores of nanoporous membrane, like nanotubules or nanorods composed of conductive polymers [14], metal nanowires [15-18], semiconductor nanowires [10], carbon nanotubes and other materials. Besides, both hollow and solid nanorods with very small diameter can be prepared while the dimension and aspect ratio of them can be completely controlled by controlling the morphology of the template [14].

Moreover, the fabricated nanostructure in the templates can be assembled into a diversity of architectures while they are inside the pores of the templates or they are freed from the membrane and collected as free standing nanostructures.

However, there are some factors that must take into consideration while choosing a technique for template-assisted synthetic method. First, to make it possible for nanostructure to grow inside the pores of nano-template the deposited material must wet the pores, second the deposition condition must be set in the way that avoids the pore blockage , and third template must be stable with respect to reaction conditions [13, 14]. There are various kinds of templates varying from mesoporous silica, mesoporous zeolite, or nano channel array of glass, but to date most of the works in the template-assisted method entail the two main types of nanoporous membrane which are as follow:

a) Track-etch polymeric membrane:

These templates will be obtained by bombarding a non-porous sheet of materials such as polycarbonate or polyester by nuclear fission and then by chemically etching

these tracks into pores. The pore size can be controlled by adjusting the etching time and the pore density can approach up to 10^9 pores cm^{-2} [13, 14] [6].

The resulting membrane will have pores in the random position which might have some intersections inside the membrane. These intersections can be problematic when the main purpose is studying the optical properties of nanostructure which are fabricated inside the nanopores of the membrane.

Figure 2.2 shows a SEM micrograph of polycarbonate membrane synthesized by track-etch method.

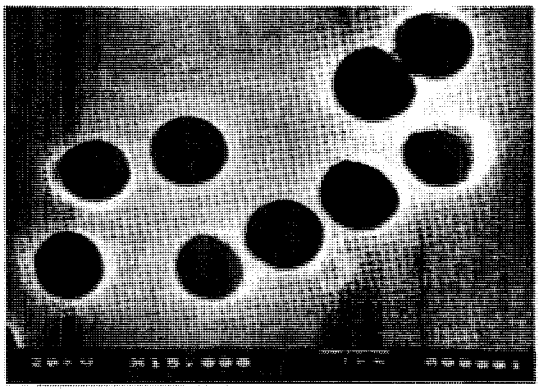

Figure 2.2. SEM micrograph of polycarbonate membrane with 1mm pore diameter [14].

b) Anodized Aluminum Oxide

Anodized Aluminum Oxide (AAO) templates can be fabricated by anodization of aluminium sheet in an appropriate electrolyte which will result in cylindrical pores with uniform arrangement in a hexagonal array [6].

In literature normally this kind of template referred to Porous Anodic Alumina (PAA) or Anodized Aluminum Oxide (AAO). AAO as a template has received considerable attention in fabrication of nanostructure for the past decade, due to its various characterization and potential to grow well ordered nanostructures. By controlling the electrolyte and anodization parameters, templates with well ordered pore arrangement with desired pores diameter and inter pore distance can be obtained [13, 19-23]. Figure 2.3 illustrates the transmission electron micrographs (TEM) of porous alumina fabricated in different agents with different anodization parameters.

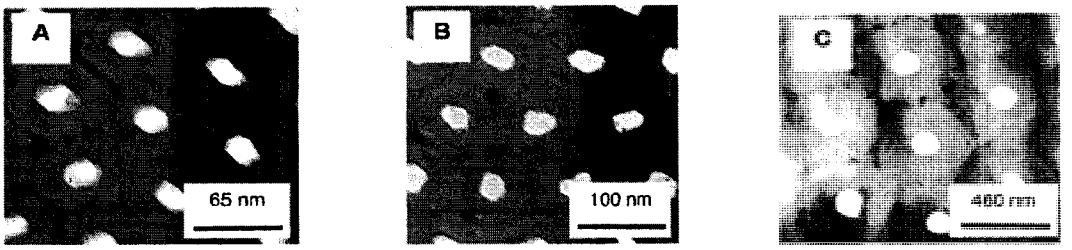

Figure 2.3. Transmission electron micrographs of porous anodic alumina prepared in (A) 25 V in 1.7 wt % H_2SO_4, (B) 40V in 2.7 wt % $(COOH)_2$, and (C) 195 V in 1 wt % H_3PO_4 [24].

In case of porous anodic alumina, unlike the track-etch membrane the pores have little or no tilt and are parallel to each other that will diminish the drawback of track-etch membrane which have intersection inside the pores of membrane. As AAO is the kind of template used in this research, the theory of AAO and affecting parameters on its morphology will be discussed thoroughly in section 2.3.

Generally, there are five main techniques to grow nanostructure materials inside the pores of AAO templates and track-etched templates that will be explained briefly in the following section.

2.2.2. Electrochemical deposition

Electrochemical deposition of a material within the pores of nanoporous membranes, in general entails the reduction of the desired material salt on the AAO template which is used as the cathode. For this purpose one side of the template must be coated by a metal film to make the conductive contact of the cathode for electroplating. As this method is known as a "bottom-up" fabricating technique, the pores start to be filled up beginning from the pores bottom. So it is obvious that the length of nanostructure can be controlled by varying the amount of material deposited and electroplating time [13, 14].

With this method both solid nanorods and hollow nanotubules can be fabricated. Many different types of metallic nanowires including copper, platinum, gold, silver, and nickel have been synthesized by this technique [13-16, 25].

The other kind of materials that can be prepared by electrodeposition in the nanoporous membranes are conductive polymers such as polypyrrole, polyaniline, or poly (3-methylthiophene) [13-15].

2.2.3. Electroless deposition

Electroless deposition involves the use of a chemical reducing agent to plate the specific material from its surrounding phase on to the surface of the template [25]. The main difference of this method with electrochemical deposition is that there is no need for the coated surface to be electrochemically conductive. The other feature of electroless deposition is that deposition of the material will start on the pore wall, therefore after short deposition time; hollow tubules will be obtained. By increasing the deposition time a solid nanowires can also be fabricated. In contrary with electrochemical deposition, in this method as there is no applied voltage, the length of nanowires cannot be controlled by the time and the final feature will result in the structure that run the complete pore diameter of template [14, 17].

With this method variety of metal nanowires such as Au, Cr, Ni, Yb, Dy, and also carbon nanotube and wide range of inorganic compounds, including $RhCl_3$, $AuCl_3$, $PdCl_2$, SnO_2, pure metals (Fe, Ni), and oxides (Sm_2O_3) can be synthesized. Figure 2.4 shows a schematic process of this method used for fabricating $LiMn_2O_4$ tubule array [13].

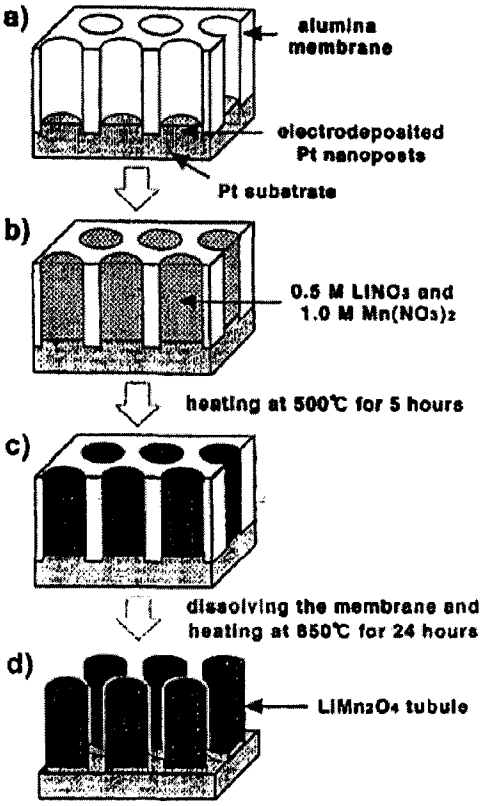

Figure 2.4. Schematic illustration of fabricating lithium-manganese-oxide tubular array by electroless deposition technique [13].

In this process, a porous alumina template was "plugged" with Pt nanoposts at the first stage (Figure 2.4.a). Then the template was immersed in an aqueous solution of Li and Mn nitrates (Figure 2.4.b). At the next stage the membrane was heated up to 500°C for around 5 hours (Figure 2.4.c), and finally the alumina membrane was removed by immersing in NaOH solution to approach tubular array of lithium-manganese-oxide [13, 25].

2.2.4. Chemical polymerization

Another template-assisted method that can be used to synthesize different conductive polymers is by polymerization the related monomer to yield tubular nanostructures. The process can be accomplished by immersing the template into the solution which contains

the required monomer and a polymerization reagent. With this process variety of conductive polymers within the pores of various templates can be synthesized.
As the polymers in general nucleate at the pore wall, so with short time deposition hollow tubules and with long time deposition solid fibres can be fabricated [13].

2.2.5. Sol-gel deposition

Sol-gel deposition involves preparation of a solution of precursor molecule to gain a suspension of colloidal particles which is known as the sol, and then a gel made of aggregates sol particles will be thermally treated to synthesize the desired nanostructure inside the pores of template. This mechanism can be conducted to create both tubular and solid nanofibrils of variety of materials such as TiO_2, ZnO and WO_3 [14].
Fig.2.5 shows SEM images of TiO_2 tubules and fibrils synthesized in alumina template via sol-gel deposition technique. This fabrication will be done by immersing the alumina template inside the sol for around 5-60 seconds. After thermal treatment, either tubule or solid fibril can be prepared. As the pore wall has negative charge and the sol has positive charge the sol will be adsorb to the pore wall and therefore tubules will be obtained after a short immersion time.

Figure 2.5.A shows TiO_2 tubules after 5seconds of immersion, Figure 2.5.B shows nanowires after 25 seconds of immersion, and finally Figure 2.5.C shows the solid fibrils of TiO_2 after 60seconds of immersion [13, 14, 21].

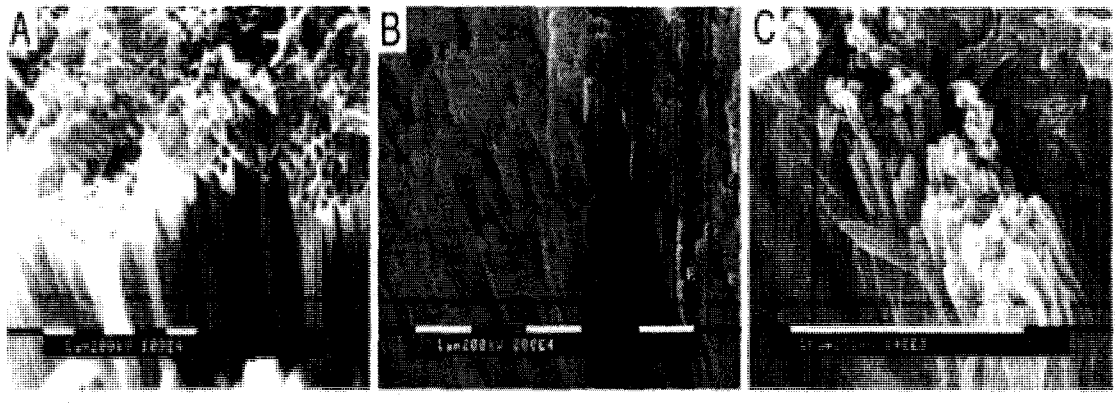

Figure 2.5. SEM images of TiO_2 tubules and solid fibrils synthesized in alumina template by sol-gel deposition technique with different immersion time. (A) Immersion time=5s, (B) Immersion time=25s, (C) Immersion time=60s [14].

2.2.6. Chemical vapour deposition

Chemical vapour deposition involves transformation of vapour phase of precursor of the desired material into the thin film or powder. This method has been used for template-assisted fabrication of carbon nano tubes from the starting material such as ethylene, pyrene ,acetylene , tripropylamine, methane , propylene , and 2-amino-4,6-dichloro-s-triazine [26]. One of the disadvantages in synthesizing carbon nanotube with this method is that the deposition rate is sometimes too fast that might block the surfaces of the pores before the chemical can transverse the length of the pores. So, to solve this problem it has been suggested [14] that alumina template must place in furnace at high temperature (700°C) and a passing gas such as ethane pass through the template. By thermal decomposition of gas inside the pore wall carbon nanotube can be fabricated. The thickness of nanostructures depends on the reaction time and gas pressure inside the chamber.

One of the other nanowires that can be fabricated via this method is gold nanotubules with concentric TiS_2 outer nanotubules. Figure 2.6 shows SEM images Au tubules together with outer TiS_2.

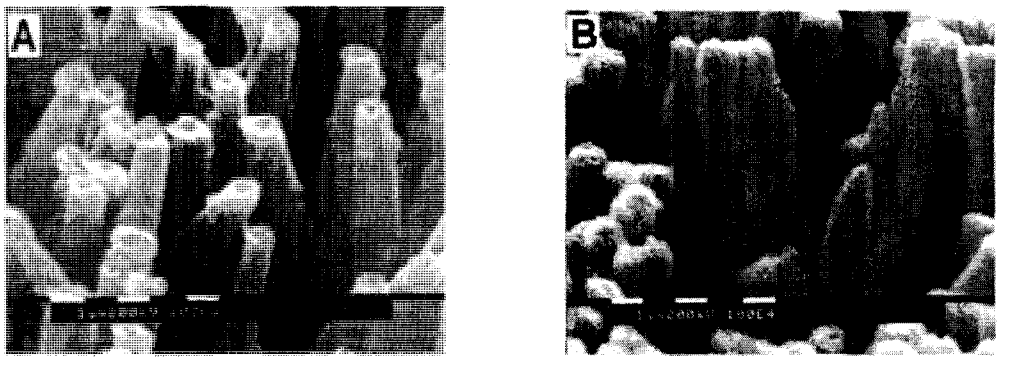

Figure 2.6. SEM images of Au tubules together with outer TiS_2. (A) Au tubules before chemical vapour deposition (B) Au tubules after chemical vapour deposition of the outer TiS_2 tubules [14].

2.3. AAO Films: background and overview

It is well known that the aluminum surface has a great affinity for oxygen. Anodic oxidation of aluminum is a process to improve this natural oxide to produce a thicker, more uniform oxide film on aluminum surface [21].

The controlled anodization of aluminum has been an industrial process since 1920 [27]. In last few decades the anodized aluminum oxide (AAO) has received increasing attraction due to its particular characters as a template to grow nanostructure materials. AAO, besides its low cost of manufacturing process, has controllable pore diameter, with extremely narrow distribution and ideal cylindrical shape. These characteristics offer a promising route to produce a large-area, ordered nanostructure with high aspect ratio templates which optimize the performance of the fabricated nano device [28] .

Generally, AAO template consists of closely packed cells of amorphous alumina in a hexagonal arrangement that can be prepared by an inexpensive process of aluminum anodization in a proper acidic environments [29]. The type of oxide film that grows on the aluminum can be divided into two different categories: barrier-type and porous-type films.

Barrier-type films composed of a relatively thin compact layer of aluminum oxide which grows on the aluminum substrate in a nearly neutral electrolyte (PH values of 5-7) and it is completely insoluble inside the electrolyte. The structure of the barrier film is mostly composed of amorphous material surrounded by microcrystalties of γ-Al_2O_3, in which intercrystallite regions contains amorphous alumina, molecular water (normally in boehmite form (AlO (OH)), hydroxyl groups, and some anion that depend on the type of the electrolyte solution [30] [21].

Porous-type films consist of an outer layer composed of a thick porous structure of alumina with the pore size of 10 nm to several hundred nm and the density of 10^9 to 10^{11} per cm^2 on top of an inner compact layer of alumina on an aluminum substrate [31].

Porous type alumina is somehow soluble in the electrolyte, therefore there is constantly a competitive reaction between growing the oxide layer and dissolution of the oxide simultaneously that creates the pores of the alumina oxide [30]. As it has been mentioned previously, the AAO can be fabricated by simply anodizing aluminum sheet in an appropriate acidic electrolyte. Figure 2.7 shows a simplified schematic of an electrochemical cell used for making AAO templates.

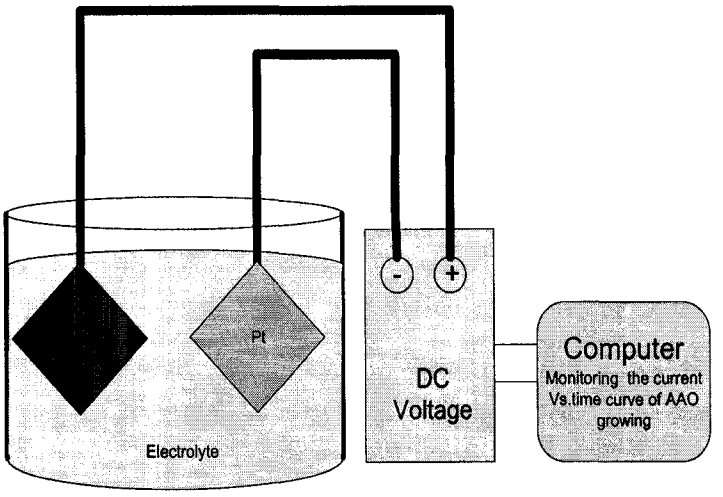

Figure 2.7. Schematic illustration of electrochemical cell used for anodic oxidation of aluminum.

The diameter and spacing of the pores on the AAO template are strongly dependent on the anodization condition such as anodization voltage, time, temperature and the type of electrolyte. As the pores morphology are considered the figures of merit in fabrication of the nanoscale devices, it is important to have a precise control on the morphology of the pores during the anodization process [1][21, 27]. Therefore, the bulk of this section will discuss about the growth mechanism of the pores and affecting parameters on their morphology.

2.3.1. Structure and Composition of porous-type AAO Films

Anodic Alumina Oxide consists of an outer region of thick, porous structure layer of alumina that lies on the thin, compact, scalloped layer of barrier layer next to the aluminum substrate [32]. Figure 2.8 shows a schematic view of the ideal structure of porous alumina.

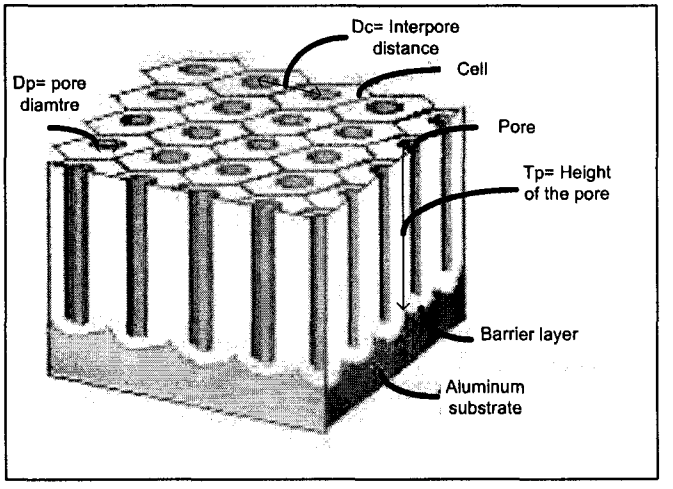

Figure 2.8. Schematic representation of ideal anodized aluminum oxide [21].

As it can be seen in Figure 2.8 ideally porous alumina has a hexagonal array of cylindrical shaped pores surrounded by amorphous alumina in which deep pores are located in the middle of these hexagonal cells [30]. D_p is the pore diameter that has a linear dependency on the applied voltage. D_c is the inter pore distance that is mainly dependant on the type of electrolyte and the voltage as well and T_p is the height of the pores that can be adjusted by controlling the anodization time.

In practice, this ideal pore arrangement is not easy to obtain, instead the pores display a more random order and they are not necessarily circular and well defined. In 1995, a remarkable breakthrough was achieved by Masuda and Fudaka [24] that made it possible to fabricate well ordered nano pores by following a two step anodization process. They found that by anodizing the aluminum in a specific electrolyte and voltage

and then stripping off the formed oxide film and re-anodizing it again, ordered nanopores with almost hexagonally domains can be produced.

The growth mechanism of the porous alumina can be divided to four steps which are: initial oxide growth, pore initiation, pore development, and steady state growth. Each step will be discussed briefly in the following section.

2.3.2. Initial oxide growth

As the voltage applies to the aluminum, the induce electric field will facilitate the growth of the oxide layer at the metal-electrolyte interface. The applied field must meet the critical current density, below which no film growth can occur at the film-electrolyte interface [20].

At the first stage there is a very thin oxide layer that has been initially grown on the aluminum substrate, so, the impedance of the specimen is very small for ionic migration. This low impedance will allow a high current density in the alumina that will produce a thicker layer of alumina on the substrate. It is obvious that as the oxide film grows, the impedance will increase and therefore the current density inside the specimen will decrease [21].

2.3.3. Pore initiation

When the oxide film grows at the metal-electrolyte interface; the initial non-uniform surface of the oxide will assist the pore initiation at the specific regions of the oxide. Figure 2.9 illustrates the schematic diagram of pore initiation during anodizing of aluminum in phosphoric acid [20, 21].

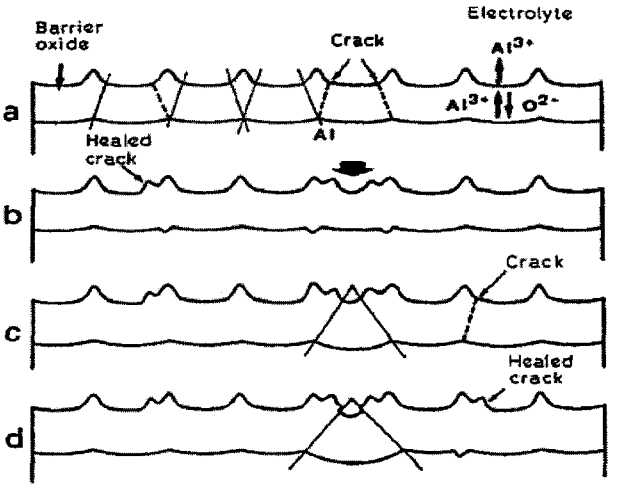

Figure 2.9. Schematic diagram of non-uniform surface of initial oxide layer: (a) Initial crack and protuberance on the oxide surface. (b) Cracks healed by oxide growth because of increased ionic mobility in cracks and consequently more surface roughening will be produced (c) The current enhanced in the thin oxide regions which reveal distorted semi-spherical curvatures (d)This curvature increases the local electric field at the oxide/electrolyte and therefore oxide dissolution rate will increase [20].

As it can be seen in Fig.2.10 the surface of alumina has a non-uniform morphology with cracks and protuberances on the outer surface of alumina (Figure 2.9.a). This uneven surface is because of the primary non-uniform thickness of the initial barrier-type oxide layer that results from the roughness of the initial aluminum surface itself. Besides, difference in the density of the alumina compared to that of bulk aluminum will induce stress on the oxide layer which cause cracks on the outer surface of alumina [20, 21]. The bumpy surface of alumina will cause redistribution of current and the current would concentre more into the thin film regions between protuberances. When the ionic mobility increases in the cracks the growth of oxide layer will be enhanced in this specific regions and therefore heal some of the cracks. This healing cracks will result in more surface roughening(Figure 2.9.b) [21].

In the thin areas between protuberances, where the current for film formation largely flows, local hemispherical curvatures with different radii will be produced. Furthermore, as the voltage augment the continual crack and heal event will make the protuberance to become wider (Figure 2.9.c) [19, 20]. As all outwardly Al^{3+} ions will be lost into the electrolyte without forming any solid film material, these initial penetration paths, will be the precursors for the ultimate development of the porous anodic film.

As it can be seen in Figure 2.9.d, local electric field will be increasing inside the curvatures and therefore the rate of dissolution in oxide/electrolyte interface will increase. Moreover, with further film growth, the ridges become more prominent. Therefore, as the overall film thickness increases the curvature of the film on surface between protuberances will be increased [20].

Figure 2.10 shows SEM images of alumina oxide anodized at 18 V_{dc} in 10% sulphuric acid in its first few seconds of pore initiation. In this Figure, dark regions represent thinner areas of the oxide while the brighter regions represent thicker areas. In the beginning regions of locally thicker oxide islands nearly tens of nm in diameter nucleates at random positions.

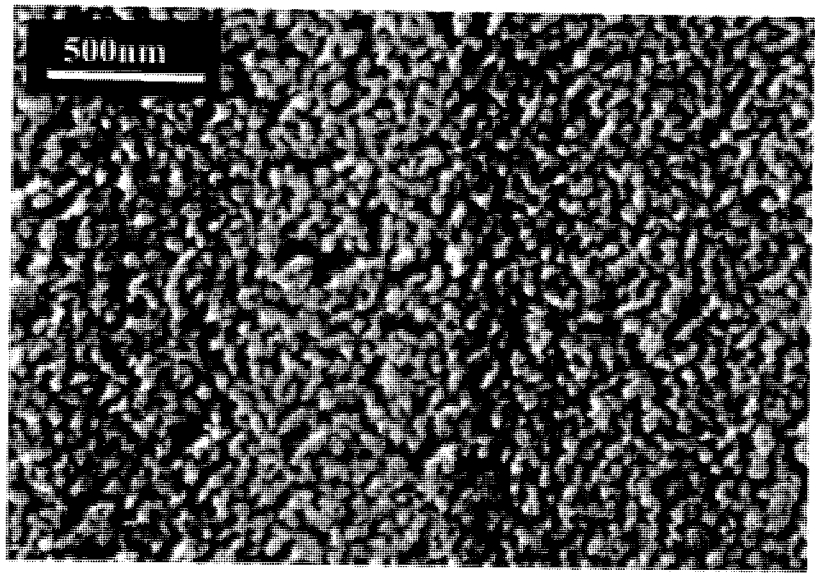

Figure 2.10. SEM images of porous alumina film anodized in 10% sulphuric acid at the beginning stage of pore development.

2.3.4. Pore development

At this step, major pores have been initiated to develop. So, there will be semi-spherical thin regions of nanopores on the oxide layer which has been nucleated at random position on the surface. With the development of penetration paths the potential distribution remains quite uniform and it will be separated within the compact region of film. Underneath of the pores bottom, the potential lines are much more concentrated, causing local increase in field strength [20]. A major parameter that facilitates the pore

development is field assisted dissolution that will be discussed thoroughly in the next section. As the local field in the beneath the tip of the penetration path increases, their development will be enhanced by field assisted dissolution; in which field assisted dissolution polarizes Al-O bonds, allows more ready Al^{3+} dissolution than in the absence of the field.

While the oxide is growing in this stage if a part of oxide layer grow thinner than the other parts, the impedance of that specific part will be less to the ionic migration and therefore more current will flow to that region and a faster oxide growth will occur in that region.

So, at this step of growth, the semi-spherical curvature of oxide/electrolyte interface that has been produced during the pore initiation process, will tailor the pattern of the pore and by the oxide growth a semi-hemispherical curvature at the metal/oxide interface will be developed [20, 21] [30]. The pore diameter and cell size are now approaching the steady state condition and pores will be propagate to the substrate by influence of field assisted dissolution that is the main factor in the steady state growth. So, to better understand the last step of pore growth, field assisted dissolution will be discussed in the next section.

2.3.5. Field assisted dissolution

Aluminum oxide (Al_2O_3) has almost ionic nature and its dissolution involves the breaking of Al-O bonds in the lattice where the product of this reaction is Al $(H_2O)_6^{3+}$ ions and water (H_2O). As it is known, any course of action which weakens the Al-O bonds in the aluminium oxide would lower the effective activation energy for dissolution and therefore will facilitate the dissolution of the alumina in the pore growth stage.

One of the important processes that will ease the dissolution is because of the presence of electric field across the oxide/electrolyte interface which is named as field assisted dissolution. Figure 2.11 illustrates the schematic diagram of the oxide film, and for simplicity it has been assumed that the oxide has a Na-Cl structure.

Figure 2.11.a shows the oxide structure near the solution before the field is applied. In Figure 2.11.b by applying the electric field across the oxide layer, the oxide structure will be polarized. At this point the field is tending to pull the O^{2-} ions into the oxide and push the Al^{3+} ions into the solution so the Al-O bonds enlarge in length.

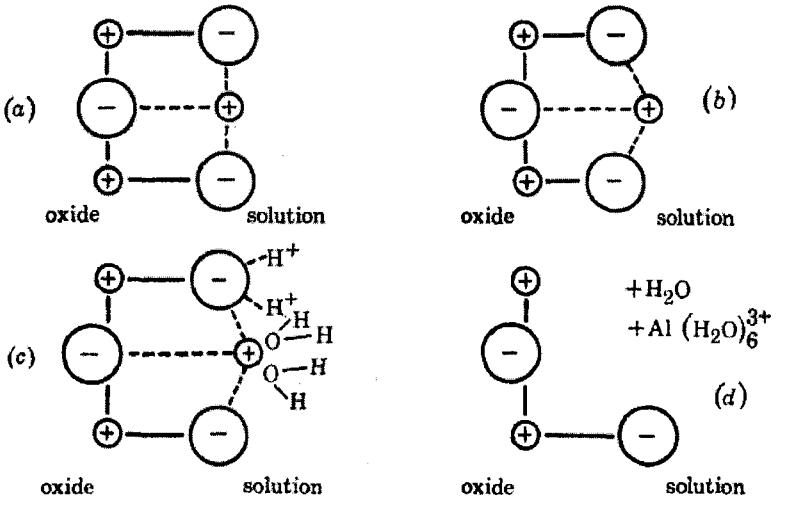

Figure 2.11. Schematic illustration of field assisted dissolution, (a) before the applied field (b) after applying field the oxide polarized (c) removal of the Al^{3+}inos (d) oxide layer after removing the Al^{3+} ions[21]

In Figure 2.11.c, the salvation of the Al^{3+} ions by water molecules and removal of O^{2-} ions by H^+ is shown which has been facilitated by the applied field. Figure 2.11.d shows the oxide layer after the Al^{3+} ions has been removed.

A single major pore with the easiest current paths through the oxide layer is illustrated in Figure 2.12. These lines can be interpreted as the lines of force of electric field as well. The configuration of these electric field lines shows that, even though the electric field lines are constant and parallel at the even parts of the oxide layer, at the base of the pores where there are curvatures, the passing current lines or the electric field lines are increasing from AE to BF.

At the pore bases the local field in bottom of the pore base BDF that determines dissolution, is larger than the field at the CAE which determines film growth. Therefore the rate of dissolution near BDF is assisted by the field to a greater extent than its growth

at CAE, and also more than elsewhere on the outer surface of the film so that the pore can be propagated and becomes surrounded by a cell [19].

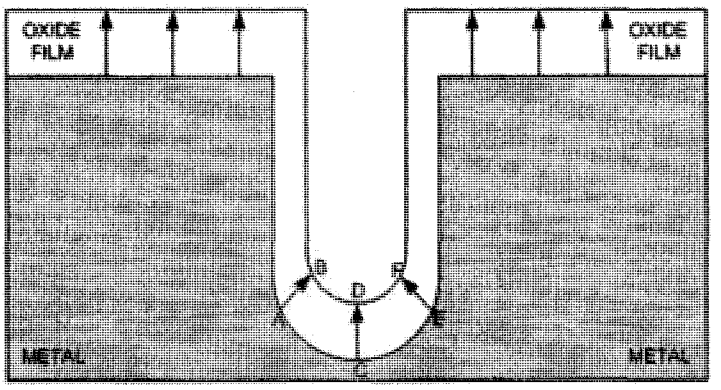

Figure 2.12. Schematic representation of a single pore and distribution of its field lines.

2.3.6. Steady state growth

For the steady state pore growth the average field across the pore base will dictate the film growth where the field assisted dissolution is the main factor that balances the constant rate of pore growth.

Figure 2.13 shows schematically three probable cases that the pore base has different radii of curvature. It has been assumed that the thickness of the oxide b, and the solid angle ω remain constant for the three cases of pores. It is also assumed that r, is the equilibrium pore base radius of curvature [19].

The applied electric field will increase in passing from the cell base to the bottom of the pores and the ratio of this increasing can be implies by the ratio of the cell base area to the pore base area which will be as follow:

$$\frac{(r_1+b)^2}{r_1^2}; \qquad \frac{(r_2+b)^2}{r_2^2}; \qquad \textit{and} \qquad \frac{(r_3+b)^2}{r_3^2} \tag{2.1}$$

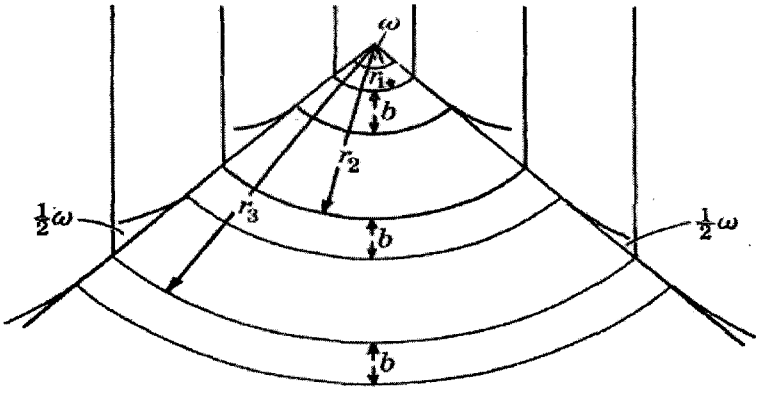

Figure 2.13. Schematic representation of single pore in alumina film and three possible pore base size, r_1, r_2, r_3 [19].

It is obvious that as the radius of curvature increases, any enhancement of the field assisting dissolution at the pore base will decrease with the ratio given in Eqn.2.1. The same process will happen if there is any decreasing in the curvature of a pore in which the enhanced electric field assisted dissolution will facilitate the pore growth and will expand the pore curvature as well. So at this stage the rate of dissolution will be balanced by local applied field everywhere in the alumina film [19].

Consequently the cell size and radius are both depending linearly on the average applied field at the pores base. In accordance with the experimental results it is found that AAO film with pore diameter varying from 5 to 500nm can be prepared by applying different voltages[21].

Under steady state condition as there is no change in the in voltage with time the film parameters will stay unchanged because of the self adjusting pore morphology by field assisted dissolution. As it has been mentioned any change in the pore diameter will affect the increasing or decreasing of the field assisted dissolution and therefore there will be a constant film growth rate in the steady state stage. In Figure 2.14 the current versus time of all four steps of pore growth and schematic diagram of these four steps is shown.

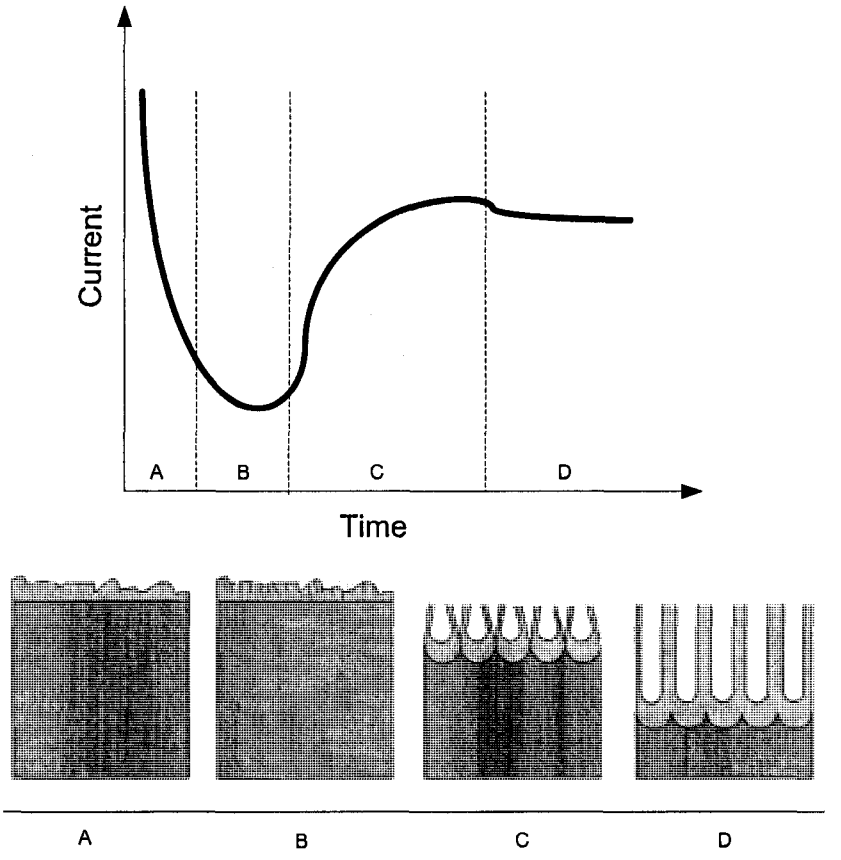

Figure 2.14. Current versus time of all four steps of pore growth and schematic diagram of these four steps.

As it can be seen in Figure 2.14, part A belongs to the first initial oxide growth of aluminum, in which a primary voltage is applied. The current starts out very high because there is only a very thin oxide layers present so the impedance is very small for ionic migration. After a few seconds, as the oxide film grows the current starts to fall down (Figure 2.14.A).

At the next stage, the current goes through a shallow minimum. The bumpy surface of alumina with cracks and protuberances will cause redistribution of current and the current would concentre more into the thin film regions between protuberances, therefore the ionic mobility increases in the cracks and and hence more current pathways start to commence. This is where; the pores start to initiate (Figure 2.14.B).

At Figure 2.14.C, as the major pores start to develop, the impendence to ionic migration decreases so the current will rise.

Figure 2.14.D, illustrates the steady state situation of pore growth. The current density takes on roughly constant value throughout the rest of the anodizing process. At this step, pores are fully developed, and growth and dissolution are occurring at roughly the same rate.

2.3.7. Ordered growth

As it has been discussed previously, not all the anodization condition will lead to well ordered pores on the alumina oxides and it more likely to produce random arrays of pores.

In 1995, a Japanese group [29] found that under the right fabrication conditions, such as appropriate forming voltages (specific for each electrolyte), proper temperature, longer anodization time, and two steps anodizing of the aluminium the pores would be well order into a hexagonally close packed.

Although it is not yet known what causes the AAO to spontaneously grow in well ordered regime under specific processing condition, there are number of setting that is known in which well ordered alumina film can be obtained.

There is an explanation by a German group in 1998 [24] that can explain the self-organization of pores inside the alumina oxide [23]. As the atomic density of aluminum in aluminium oxide is by a factor of two lower than in metallic aluminum, one possible basis of this force between neighbouring pores is because of the mechanical stress related to the expansion during oxide formation at the metal/oxide interface.

At steady state of pore growth, migration of oxygen ions (O^{2-} /OH^-) from the electrolyte to the oxide layer and also Al^{3+} ions which migrate at the same time through the oxide layer to the solution, the pores will grow perpendicular to the surface. It is known that by changing the applied voltage and electrolyte concentration, the amount of aluminum transforming to the oxide can be varied, therefore the relative transformation of Al^{3+} and also O^{2-}/OH^- ions are also function of applied voltage which will make change in the stress at the metal/oxide interface [21]. The volume expansion factor was calculated by this group, and it was found that this expansion differs from 0.8 to 1.7 in different anodization conditions.

It was found that pores with maximum well ordered morphology can be obtained whenever the anodization condition were set to moderate the volume expansion by a factor of 1.4 [23, 24]. It is also important to know that well ordering of pores will be occur through the time under appropriate anodizing condition which means, although pore might initiate randomly at the first step but the will become gradually well ordered at the metal-oxide interface as the time passes.

Chapter 3: Characterization and measurement techniques

3.1. Atomic Force Microscope (AFM)

The Atomic Force Microscope (AFM) was invented in 1986 by Binnig, Quate and Gerber [33]. AFM ,like the other measurement instruments such as Scanning Probe Microscopy (SPM) or Scanning Tunnelling microscopy (STM), consists of family of microscopy forms in which a sharp probe will scan across the surface of desired sample and generate a three dimensional image of the sample [34].

The AFM consists of a microscale cantilever made of silicon or silicon nitride, which has a sharp tip (probe) in the range of nanometre at the end of the cantilever that is responsible for scanning the surface of specimen [32, 35]. Figure 3.1 shows schematic overview of main components that are used in an AFM for scanning and getting an image of the sample.

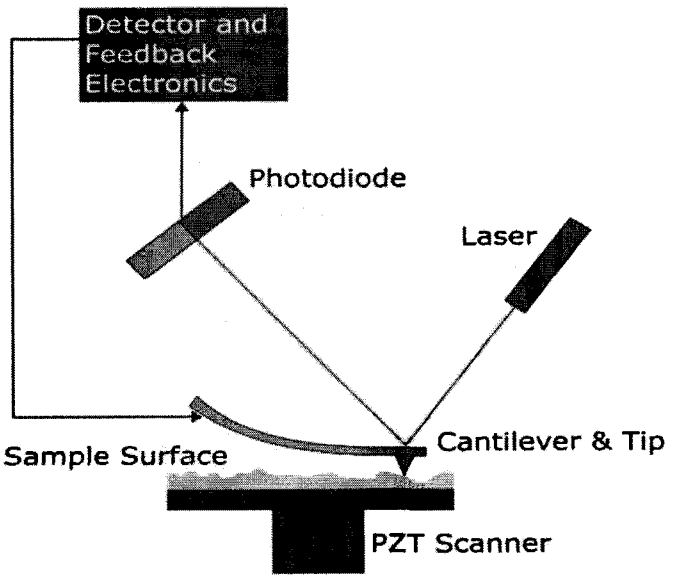

Figure 3.1. Schematic illustration of AFM system [32].

The principal work of the AFM is to measure the force between its probe and the surface of the sample. As it can be seen in Figure 3.1 the sharp tip located at the end of the cantilever will scan the surface of the sample, while a laser beam from a solid state diode is reflected off the back of the cantilever. This optical beam will be collected by a position sensitive detector (PSD) consisting of two closely spaced photodiodes.

When the cantilever moves up and down, one photodiode will receive more light than the other photodiode where an output signal will be generate; obviously this signal will be proportional to the deflection of the cantilever. So, in this way PSD can sense the movement of cantilever.

While the tip is scanning on the surface of the sample, if it remains at a constant height with regard to the surface of the sample, there might be collision between the surface of the sample and the tip that might cause damage to the tip. So, a feedback unit is designed to adjust the distance of the tip in the Z direction to the surface of the sample to keep a constant force between the tip and the surface of the sample. For this purpose in some models, the scanner that is constructed via piezoelectric material will move the sample with regard to stationary tip, and in the other models the sample is stationary while the piezoelectric scanner moves the tip [32, 34]. Depending on the type of application, AFM can operate in three main modes of operation named contact mode, tapping mode, and non-contact mode.

3.1.1. Contact mode

In the contact mode AFM operates by scanning the surface of the sample via the tip that is attached to the end of the cantilever while contacting the surface of the sample. The change of cantilever deflection is monitored by PSD [34].

In this mode, the feedback loop will maintain a constant deflection between the cantilever and the sample by moving vertically the scanner at each (x, y) data point to keep a setpoint deflection. With a constant cantilever deflection, there will be a constant force between the tip and the surface of the sample, in which this force can be measured by Hooke's law:

$$F = -Kx \tag{3.1}$$

Where F is the applied force, K is the spring constant, and x is the value of the cantilever defection [34]. As the scanner moves vertically at any specific (x, y), the data point will be stored in the computer and a topographic image of the sample will be obtained [34].

3.1.2. Tapping mode

In the tapping mode, the tip is still in contact with the sample surface but it just lightly "taps" on the surface by the oscillating cantilever. In this mode, the feedback loop keeps constant oscillation amplitude during the imagining

To make a topographic image of the sample surface, the vertical position of the scanner at each (x, y) data point will be stored in the computer. By keeping constant oscillation amplitude, the interaction between tip and the sample has a constant value during the operation. This mode, can take place in both ambient and liquid environment [34]. Tapping mode has a lower scan speed comparing to the contact mode, but it has the advantage of applying less force to the specimen, and consequently result in less damage to soft samples.

3.1.3. Non-contact mode

In this mode the tip does not contact the sample surface, but it only oscillates above the adsorbed fluid layer on the surface during the scanning. The cantilever will oscillate at a frequency that is a little bit above the cantilever's resonance frequency with amplitude of less than 10nm to get an AC signal from the cantilever.

Scanner will move vertically at each (x,y) data point by the feedback loop to maintain a constant oscillation amplitude or frequency until a "setpoint" amplitude or frequency is achieved. To obtain a topographic image of the sample surface the distance of scanner at each (x, y) data point will be stored by the computer [34].

This mode has a very limited application because only works on extremely hydrophobic samples, where the adsorbed fluid layer is minimum cause if the fluid layer is too thick the tip might trap in the adsorbed fluid layer and lead to an unstable feedback loop. Besides, this mode has the lowest scanning speed comparing to the contact mode, and tapping mode [34].

3.1.4. AFM measurements

The type of AFM which was used during this research is Multi Mode AFM, and the model is AFM-2. The scanner is As-130 (J) with a maximum scan size area of 125 μ m$\times$125 μ m and it has a vertical size of 5.0 μ m in the tapping mode.

As the imaging of the sample in this research was obtained via tapping mode, so the specification of the silicon cantilever and the tip used in this mode is illustrated in table 3.1.

Table 3.1. Tapping mode etched silicon probe (TESP) specification.

Model of AFM Tip	TESP
Tip Material	
Cantilever Specification	Thickness: 3.5-4.5 μm, Length:110-140 μ m, Width : 25-35 μm
Resonant Frequency	
Spring Constant	K: 20-80 N/m

Figure 3.2 shows a photograph of the AFM instrument which was used in this research.

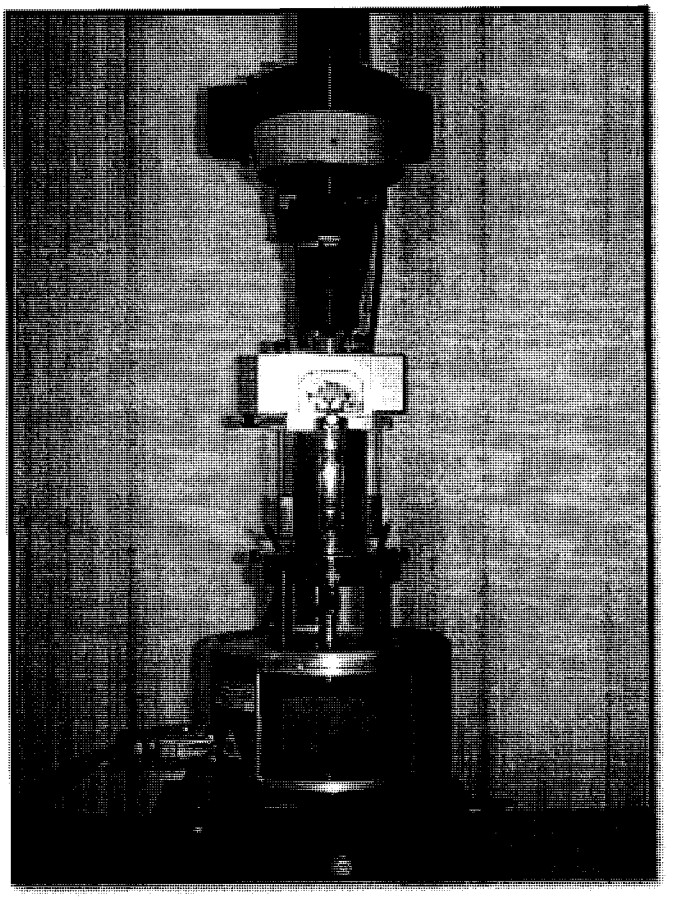

Figure 3.2. Multi Mode AFM, model AFM-2 with As-130 (J) scanner

3.2. Scanning Electron Microscope (SEM)

Scanning Electron Microscopic (SEM) is one of the other widely employed instruments related to our application of interest which is studying the film and surface morphology and structure [36].

SEM is an imaging method in which electrons rather than light is used to form an image. The SEM produces images of high resolution which allows examination of closely spaced features at a high magnification. A comparison of the obtainable resolution of SEM with other methods is illustrated in table 3.2.

Table 3.2. Comparison among resolution of eye and various microscopy methods[37].

Technique	Limits	Resolution
Eye	Retina	700,000 Å
Optical microscope	Diffraction of light	3000 Å
Scanning electron microscope	Diffraction of electrons	30 Å
Field ion microscope	Atomic size	3 Å
Transmission electron microscope	Diffraction of electrons	1 Å
Near-field scanning probe microscopies	"Aperture" size	0.1 - 100 Å

There are two main limitations imposed on the imagining with the SEM [37]. First, the minimum size of sample should be at least 0.1mm and second the sample must be conductive or coated with thin conductive layer.

A schematic of the typical SEM is shown in Figure 3.3. The working mechanism of SEM is based on electrons instead of light, so a beam of electrons is generated in electron gun. In order to explain the electron gun in more detail, the gun is shown in Figure 3.4.

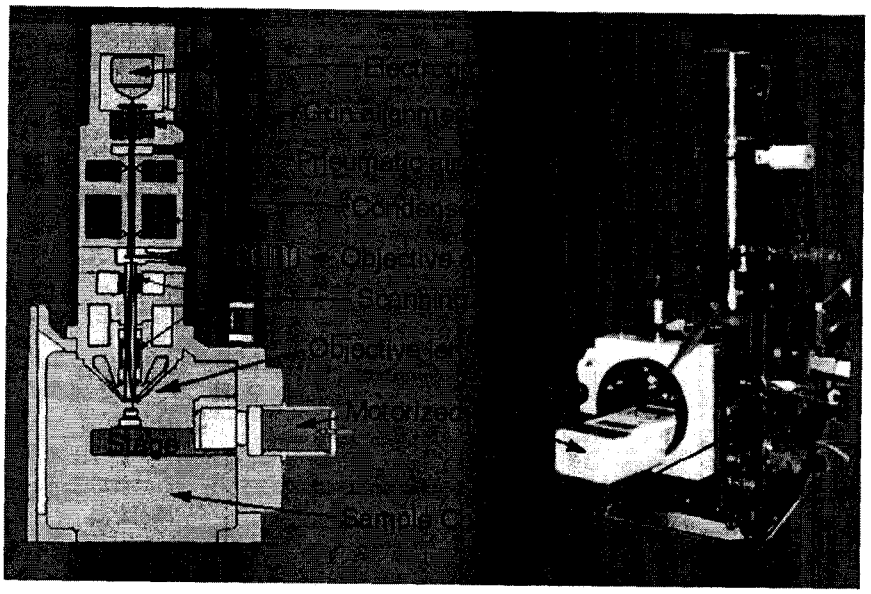

Figure 3.3. Schematic view of the typical SEM [23]

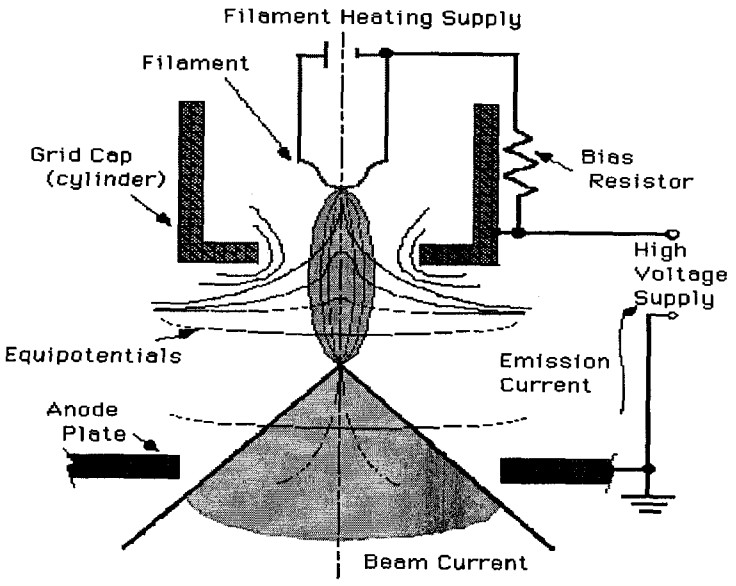

Figure 3.4. Schematic image of the electron source in the SEM [23]

By applying voltage to the heating up tungsten or LaB6-cathode it will stimulate the gun to emit electrons. Electrons would accelerate to an anode which is positive with respect to the filament and consequently induces powerful attractive forces.

Accelerated electrons will be focused into a beam with a tiny tip (typically 1Å in diameter) by two condenser lenses. As the electron beam is passing through the sample surface, it will be deflected by a magnetic field. By changing the voltage of scan generator the electron beam can sweep a rectangular area of the specimen surface linearly or in a raster fashion [36].

Electron beam will hit the sample with energy ranging from a few keV up to 50keV. While electrons are impinging inelestically to the specimen, they will lose their energy and transfer it to other atomic electrons and to the lattice. By means of energy transfer, a distribution of excited electrons is formed which manage to leave specimen with an energy spectrum.

Detection these secondary electrons is common imaging mode that applies to the SEM. These secondary electrons are very low energy electrons which originate from the subsurface depth of several angstroms. A detector consists of scintillator/photomultiplier combination will detect these electrons [36].

3.2.1. SEM Measurements

The model of SEM which was used in this research is S-4700. A photograph of S-4700 is depicted in Figure 3.5.

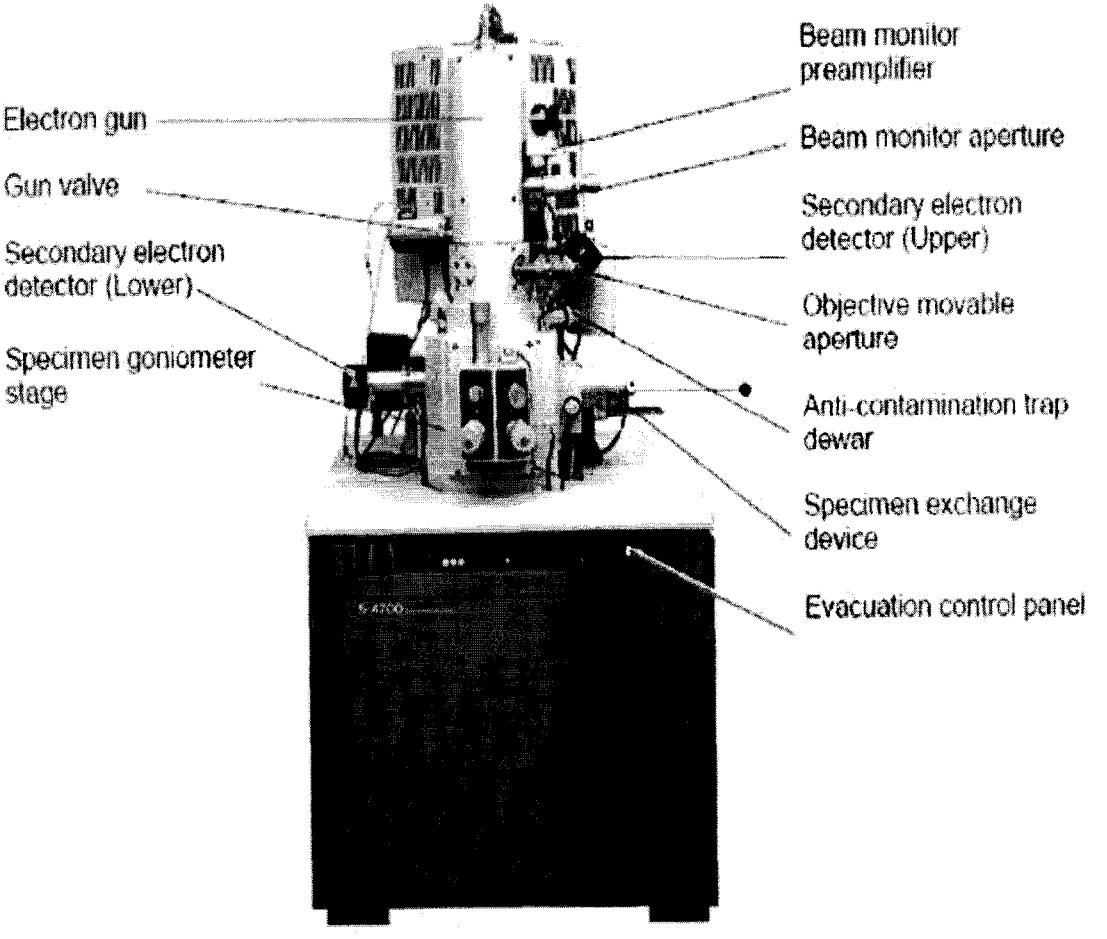

Figure 3.5. S-4700 Scanning Electron Microscopic [38]

Figure 3.6 illustrates the appearance of the specimen stage.

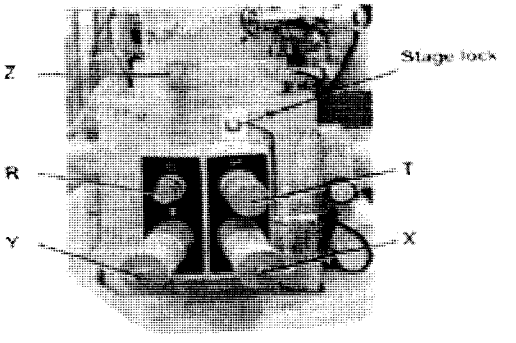

Figure 3.6. Specimen stage of S-4700 [38]

The functional operation and specification of each part is as follow:

X Control: Moves specimen in X direction with a range from 0 to 25mm.

Y Control: Moves specimen in Y direction with a range from 0 to 25mm.

Z Control: Moves specimen in Z direction or shifts working distance (WD) with a range from 1.5 to 26.6 mm. (X-ray analysis position is at 12mm working distance)

R Control: Rotates specimen through 360° (continuously variable)

T Control: Tilts specimen within a range from -5° to 45°.

Absorbed current measuring terminal: Measures beam absorbed current on specimen (normally used specimen applied terminal)

Stage Lock Switch: Used for locking the specimen stage to reduce vibration influence.

3.3. X-ray Diffraction (XRD)

X-ray diffraction (XRD) is a non-destructive technique to obtain detail information about chemical composition, crystal orientation, and other structural parameters of different materials [39]

The main idea of XRD operation comes from the Bragg's law. In 1913, Bragg developed a relationship to describe why the cleavage faces of crystals appear to reflect X-ray beams at certain angles of incidence (θ) [40].

Any crystal lattice has a regular three-dimensional distribution of atoms in which the atomic arrangement forms a series of parallel planes by a constant distance (d). Any specific material has a natural d spacing and in each crystal, there are numerous planes with different orientation and d spacing.

According to Bragg's law, when a monochromic X-ray beam with wavelength λ is projected to crystal lattice of any material (Figure 3.7) constructive interference will happen if the distance traveled by the reflected rays from successive planes are

equal to any integer value of the wavelength (λ) . Figure 3.7 shows a constructive interference of incident x-ray rays of two successive crystal planes.

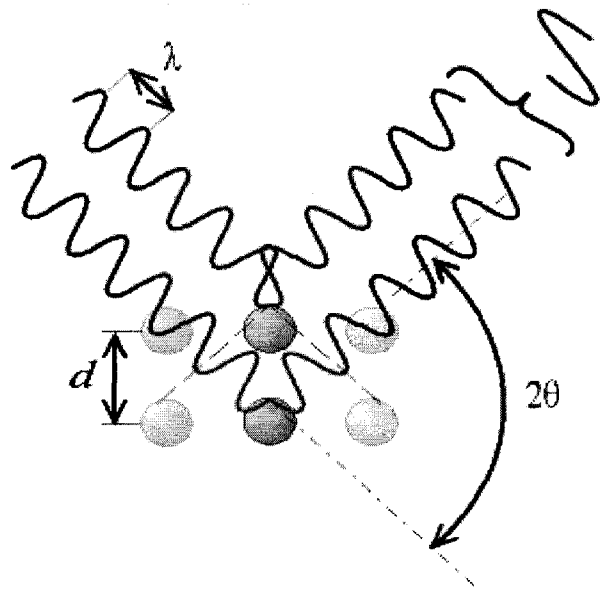

Figure. 3.7. Constructive interference of incident rays of two successive crystal planes [40].

The Bragg's law can be expressed by:

$$n\lambda = 2d \times \sin\theta \tag{3.2}$$

In which, n is an integer number, λ is the wavelength of incident waves, d is the distance between the parallel planes of crystal lattice, and θ is the angle between the incident ray and the scattering plane [40].

Therefore the possible θ values receives from reflection will show the unit cell dimension and the intensities of the reflections will be determined by the distribution of electrons in the unit cell.

A pattern will be obtained by plotting the angular positions and intensities of the diffracted x-ray peaks that this pattern will show the detailed characteristics of the sample.

Chapter 4: AAO fabrication, results and discussions

4.1. Preparation of AAO

The following section presents work on fabrication of Anodized Aluminum Oxide (AAO). In the fabrication process, optimized condition has been considered to obtain AAO films with well ordered morphology for the use of template to fabricate metallic nanowires inside them.

To start the fabrication, the Al foil substrates were subjected to various initial treatments, in order to optimize the synthesizing of AAO. Then aluminum sheet was electropolished to acquire Al foil with smooth surface. Then, the aluminum foil was anodized under different anodization conditions (various electrolytes, temperature, anodization time, and voltage).

After second anodization, the AAO were subjected to different methods to detach the porous alumina from its aluminum substrate to obtain open thorough AAO template. The detailed preparation process is illustrated in the following section.

4.1.1. Al foil pre-treatment

High purity (99.999%), 0.5mm thick aluminum foils were cut into small strips with the dimension of 1 cm×3cm. As the Al foils (provided form Sigma Aldrich) has deep scratches on them, there were first mechanically polished to obtain a smooth surface and then they were followed by further pre treatment process and electrochemical polishing. The Al strip was mounted on a custom made substrate for easier handling while it is mechanically polished with polishing machine. Figure 4.1 shows the aluminum foil mounted on the custom made substrate.

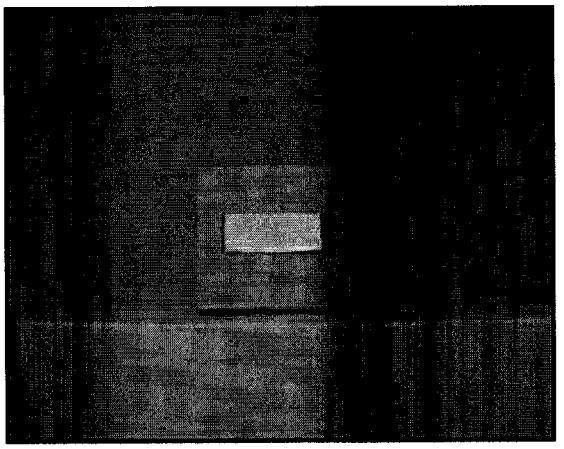

Figure 4.1. Al strip with a dimension of 1cm × 3cm, mounted on a wooden substrate.

The Al foil was mechanically gridded by sand papers with the grit of 240, 320, 400, and 600 respectively. After that, the grinded Al strip was mechanically polished by very smooth sand papers with grit of 800 and 1200. The polished Al was degreased in acetone, methanol, and DI water, followed by a cleaning step consisting of 5% NaOH solution for 30 seconds at room temperature. Then the sample was rinsed with de-ionized water for five minutes.

By mechanical polishing, deep scratches of aluminium foil are removed, but there are still some defects and protuberance of the surface. To obtain mirror like surface of aluminum, an electrochemical polishing step must be followed.

4.1.2. Electrochemical polishing

Electropolishing, is electrochemical procedure in which bumpy surface of the metal will be removed by anodic dissolution [27]. The main difference of electropolishing and anodizing of aluminium is that as the formation and rapid dissolution of the oxide layer happens simultaneously, the dissolution tends to smooth out surface irregularities with mirror like finishing. Electropolishing will be done by creating an electrochemical cell the same as Figure 2.7 in which the aluminum sheet is the anode. When a DC voltage is applied, the electrical charge will force the metal ions to be dissolved into the electrolyte. The key factor of this process is the difference in current density on the bumpy level of

the surface, where the current density is greater at the protuberance with uneven points that can dissolve faster and result in a smooth and even surface [41] .

The electropolishing of aluminum was accomplished in an electrochemical cell, in which aluminum sheet was connected to the positive terminal or anode and a platinum sheet was connected to the negative terminal as the cathode. To optimize the electropolishing of the aluminium sheet was cut to smaller pieces with the dimension of 1×1 cm. One side of the aluminum was covered with nail polish to improve the electropolishing on only one side of the sheet which will be then anodize to grow oxide on it. The electrolyte was a mixture of $HClO_4$ and EtOH (v/v 1:5 of $HClO_4$/EtOH with acid concentration of 60%).

Different anodization conditions were carried out and the best electropolished surface were obtained with $20V_{DC}$ at $1C^{o}$ for 5 minutes.

After the electropolishing, the aluminum sheet was cleaned thoroughly in DI-water and then it was annealed at 500 C^{o} under nitrogen ambient, for around three hours to decrease the mechanical stress in the aluminum film. After these pre-treatment processes, the aluminum sheet was subjected to electrochemical anodization to grow alumina on its surface.

4.1.3. Aluminium anodization (First step)

This step consist of anodizing the aluminum sheet in acidic solution such as H_2SO_4, $H_2C_2O_4$, H_3PO_4, NH_2SO_3H, or H_2CrO_4 [27]. The process was carried out while the electrochemical cell is kept in a constant temperature with a specific voltage. To achieve this condition the electrochemical cell was kept inside RM6 LAUDA recirculating chiller. Figure 4.2 shows a photograph of electrochemical cell fixed in the RM6 LAUDA chiller. The temperature was set in accordance with the type of electrolyte and applied voltage to optimize the well ordered AAO pores morphology. The aluminum sheet was connected to the positive terminal as the anode and a platinum cathode was connected to the negative terminal. The DC power supply (Keithly 2400) is also connected to the

computer and the anodization time and applied voltage were controlled by the LABTRACER software, while the current versus time graph of anodization were plotted.

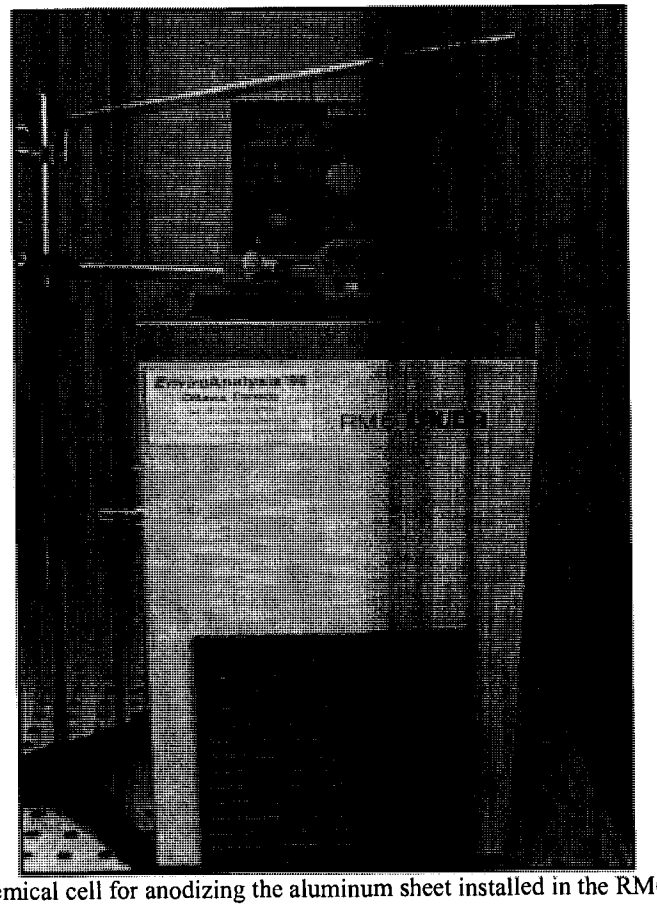

Figure 4.2. Electrochemical cell for anodizing the aluminum sheet installed in the RM6 LAUDA chiller and connected to a DC power voltage.

As the DC voltage applied the oxide will start to grow on the aluminum surface. The reaction at the metal/oxide interface or anode is:

$$Al \rightarrow Al^{3+} + 3e^{-} \tag{4.1}$$

The possible reaction at the pore bottom / electrolyte interface is water splitting:

$$2H_2O \rightarrow O^{2-} + H_3O^{+} \tag{4.2}$$

The reaction which occurred at the platinum terminal (cathode) is hydrogen releasing:

$$2H_3O^+ + 2e^- \rightarrow 2H_2O + H_2 \quad (4.3)$$

The anodization was carried out in two different electrolytes with their specific voltage. First the electrolyte was 10% sulphuric acid, with varying voltage from 12 V_{DC} to 32 V_{DC} for two to three hours. Second the anodization agent was 0.3 M oxalic acid with varying voltage from 35 to 60 V_{DC} for around 12 to 15 hours. The best results were obtained at 18 V_{DC} for sulphuric acid and 40 V_{DC} for oxalic acid.

As it has been discussed in the theory of alumina oxide film, the pore diameter and interpore distance are linearly proportional to the applied voltage.

To obtain the optimize operation temperature; anodization was carried out in different temperatures, varying from 5C° to 25C° for both electrolytes. The dependence of pore morphology was not a direct dependant on the temperature. With only one step of anodization, not well ordered pores morphology can be obtained.

4.1.4. Ordered pores (Second step of anodization)

As it has been discussed, after the first anodization step in acidic agent AAO with random pores on the surface will be synthesized. To grow self standing nanowires without any collision, one must fabricate alumina template with well ordered pores in which the nanoholes are parallel to each other.

Figure 4.3 shows schematic illustration of fabrication of alumina templates with well ordered pores. Figure 4.3.A depicts random pores of alumina after the first anodization. Therefore, the alumina will be removed from the aluminum substrate (Figure 4.3.B) by leaving behind periodic concave patterns in the aluminum surface. Then, these ordered nano dimples will serve as nucleation pattern for the second anodization step that will result in well ordered nanopores (Figure 4.3.C) [21].

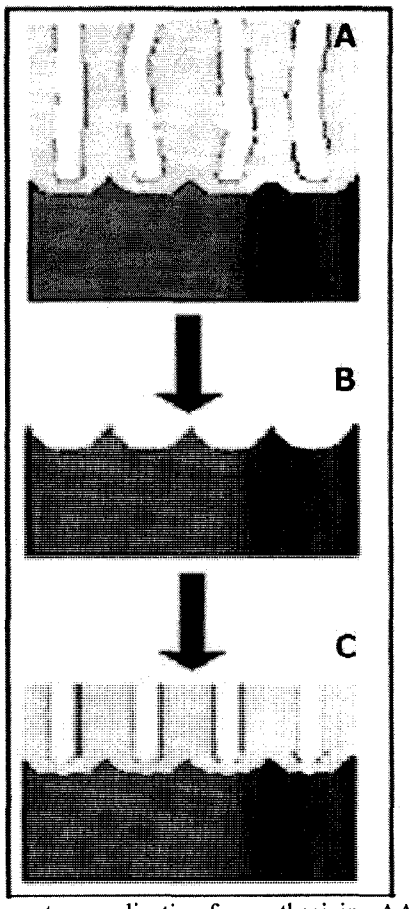

Figure 4.3. Schematic process of two step anodization for synthesizing AAO with well ordered pores [21].

For this purpose, the alumina film will be removed by a solution of phosphorochromic acid (6% H_3PO_4, 1.8% H_2CrO_4) at 60 C^o during two hours.

After removing the alumina, aluminium film will be anodized again, with the same anodization condition (temperature, voltage, and electrolyte) as the first step, but with a shorter anodization time. After this step, well ordered pores can be obtained. For sulphuric acid the second anodization was carried out for around 1 hour to 3 hours and for oxalic acid the second anodization was carried out from 1 hour to 6 hours.

The AAO prepared after the second anodization, is subject to further optional process to remove the remaining aluminum and the insulating barrier film at bottom of the pores. This step depends on the application of the template. As for the purpose of this research, an open thorough template is needed the further treatments were considered as well.

4.1.5. Preparing open thorough alumina template

There are several chemical solution in which the remaining aluminum can be removed such as $HgCl_2$, $CuCl_2$, $SnCl_4$ [42]. In this research saturated $HgCl_2$ was used to remove the aluminum substrate form the oxide film. To prepare saturated $HgCl_2$, the mixture of mercury dichloride and water was heated up to $50C^{o}$ to help $HgCl_2$ to dissolve completely. Then, the entire sample was immersed in the saturated mercury chloride for around three to four hours. It is obvious that etching time is directly dependant on the remaining aluminum. After about one hour the sample was cleaned with DI-water and immersed again in the saturated mercury chloride. This removing and replacing were carried out several times to remove the aluminum substrate completely.

To remove the insulating barrier film, there are several approaches that can be considered. This layer can be thinned gradually by reducing the anodization voltage step by step but it will not remove completely. Tian et al [43] used a reverse biasing voltage at the end of the second anodization step to thinning the barrier film , and the remaining barrier layer was removed by milling with a neutralized Ar ion beam. Although this approach was successful, but is very complex and time consuming process. There is also another technique in which the alumina film can be detached from its Al substrate by electrochemical anodization of template in 70% $HClO_4$ acidic solution with $45V_{dc}$ for around 3-4 seconds. It has been reported that via this technique the rate of oxide dissolution will increase drastically and the barrier layer will dissolve in a few seconds. By dissolving the barrier layer the alumina template will detach from its aluminum substrate resulting and open thorough AAO membrane [42].

The method which was used in this research was chemical etching of alumina template in a 1% phosphoric acid. After removing the aluminum substrate in the saturated mercury chlorides, the entire sample was immersed in a 1%phosphoric acid for 65 minutes in the room temperature to remove the barrier layer. This step must be done very carefully, because as the immersing time increases the pores will start to widen. Therefore, the pores can also be tailored by adjusting the pore widening process. As the

morphology and spacing of the pores has been developed during the two steps anodization, at the end of the process by immersing the template inside the phosphoric acid with different time, templates with different pore diameters can be obtained.

4.2. AAO template: Results and discussions

As it has been explained in the previous section, anodization of aluminum was carried out in both oxalic and sulphuric acid. Figure 4.4 illustrates a typical current vs. time curve for the first 100seconds of anodization of 1cm×1cm aluminium sheet inside 0.3 M oxalic acid. The total anodization was conducted under 40 V_{DC} for around 16 hours at 3C°. This curve is almost agreed with the schematic curve which has been explained in the previous section.

As it can be seen in Figure 4.4, when the initial voltage applied, the current starts out very high because there is only a very thin oxide layer and the impendence is very small for ionic migration. As the oxide starts to grow, the current starts to go to shallow minimum. When the pores start to initiate, more pathways will be created for current; therefore a little rise can be seen after 20 second of anodization.

After 60 second, the pores are fully developed and a steady state situation is developed where the current density takes on a roughly constant value throughout the rest of the anodizing process. In this stage, the growth and dissolution are going nearly with the same rate.

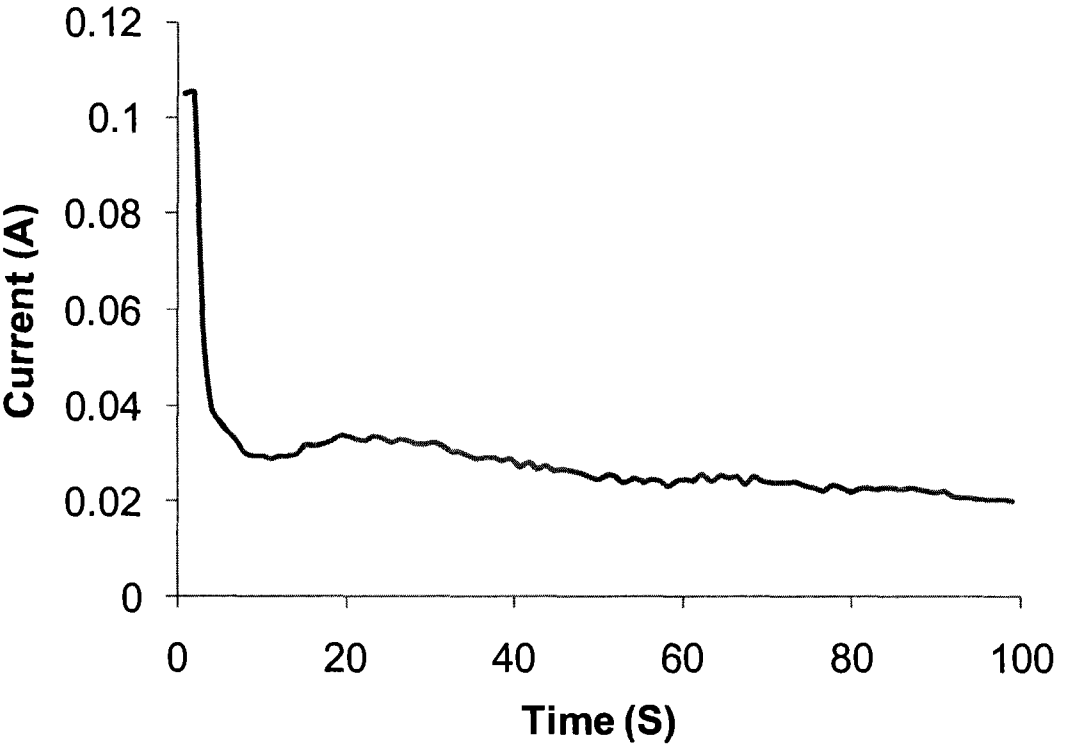

Figure 4.4. Current versus time of AAO template fabricated in 0.3 M oxalic acid, under $40V_{DC}$ after first 100 seconds of anodization.

4.2.1. SEM study of AAO film

To enhance the fabrication of AAO template, the Al foil is subjected to some pre-treatment. Figure 4.5 shows a SEM micrograph of Al foil before any treatment. Figure 4.6 shows the SEM result of Al foil after mechanical polishing, and Figure 4.7 shows the SEM image of Al foil after electrochemical polishing.

As it can be seen in Figure 4.6 deep scratches of aluminium foil has been almost removed by mechanical polishing, but there is still some defects and protuberance on the surface. Therefore the treatment will be followed by electrochemical polishing as well.

Electropolishing was carried out in $HClO_4$ and EtOH (v/v 1:5 of $HClO_4$/EtOH with acid concentration of 60%).

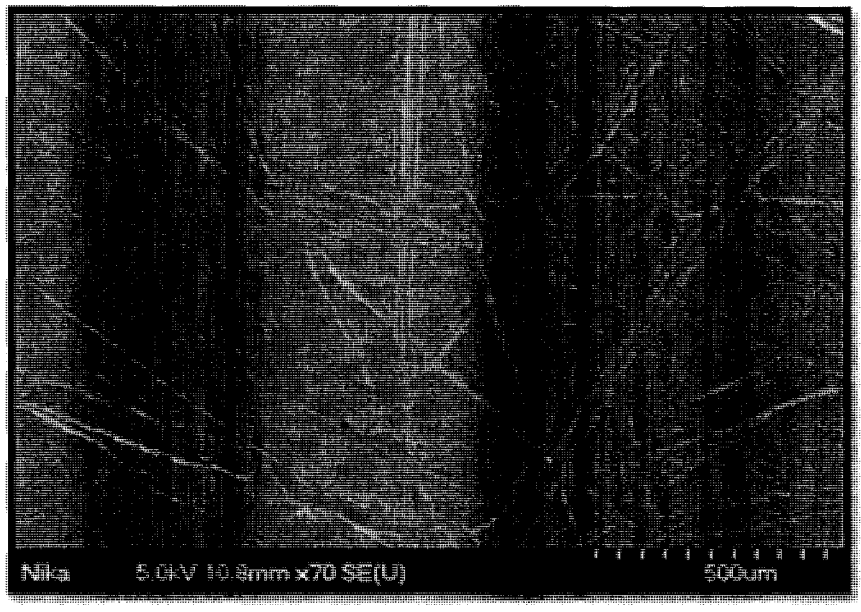

Figure 4.5. SEM image of Al foil before any pre-treatment.

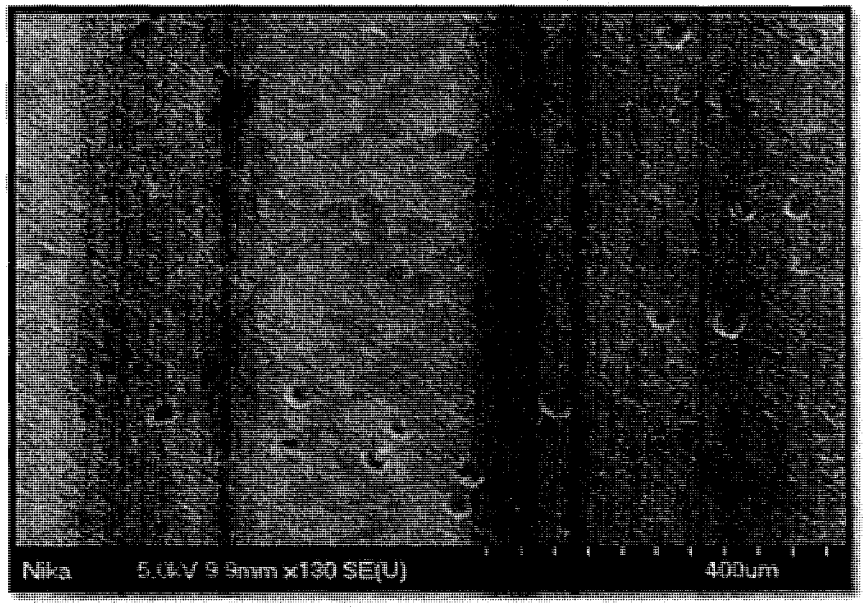

Figure 4.6. SEM image of Al foil after mechanical polishing.

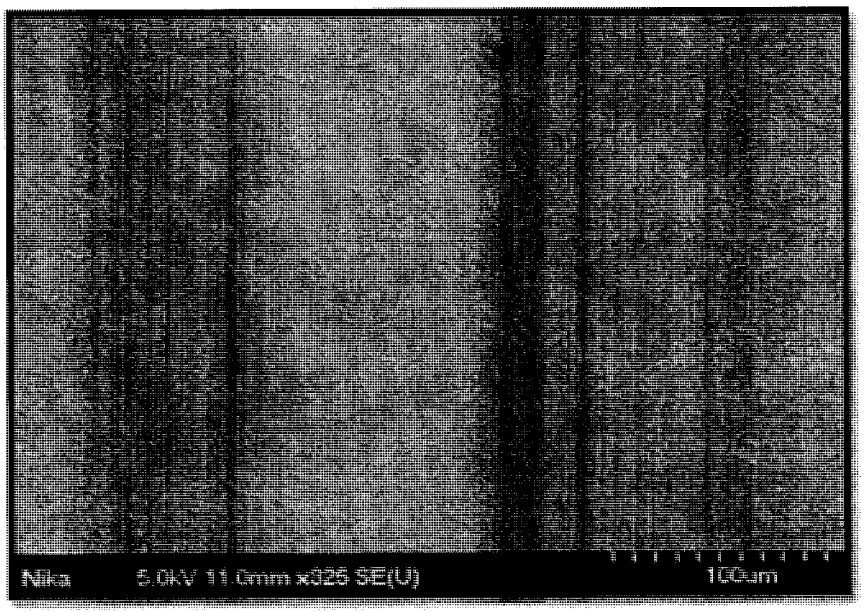

Figure 4.7. SEM image of final mirror like surface of aluminum sheet after electrochemical polishing .

It can be seen in Figure 4.7 all the scratches and defects on the aluminum surfaces have been removed by this process.

After initial pre-treatment, the anodization was carried out in 10% sulphuric acid, with varying voltage of $12V_{DC}$ to $24V_{DC}$ to obtain the best result.

Figure 4.8 illustrates SEM image of AAO template fabricated with $12V_{DC}$, two hours for the first anodization in $10C^{o}$. After removing the alumina by phosphorochromic acid, the second anodization was conducted for 90 minutes with same condition as the first step. The aluminium substrate is removed with saturated $HgCl_2$.

It can be seen in Figure 4.8, the pores size are ranging from 20-24 nm and are not very uniform.

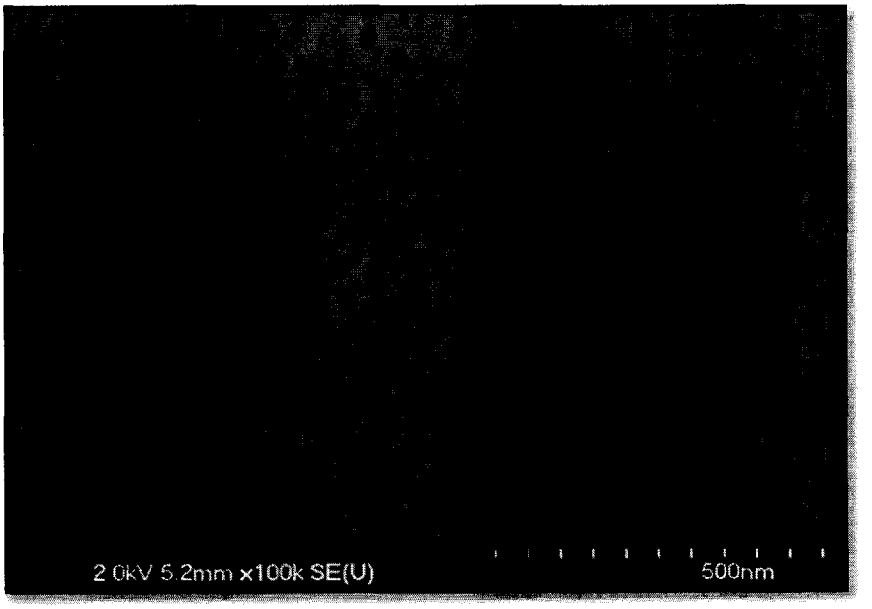

Figure 4.8. AAO template fabricated in sulphuric acid with $12V_{DC}$, for two hours at $10C^{o}$.

To maximize the uniformity of the pores, the experiment was held out with $15V_{DC}$, $18V_{DC}$, $20V_{DC}$, and 24 V_{DC} as well in the same electrolyte. The best results were obtained in $18V_{DC}$ and $24V_{DC}$ in 10%sulfuric acid with interpore distance of 50nm and 60nm respectively.

Figure 4.9 shows SEM image of AAO template fabricated with $18V_{DC}$ in $7C^{o}$ after its first step of anodization. It can be seen that the pores are randomly distributed, therefore the second anodization step were carried out for two hours. Figure 4.10 shows the SEM micrograph of AAO template after its second anodization step.

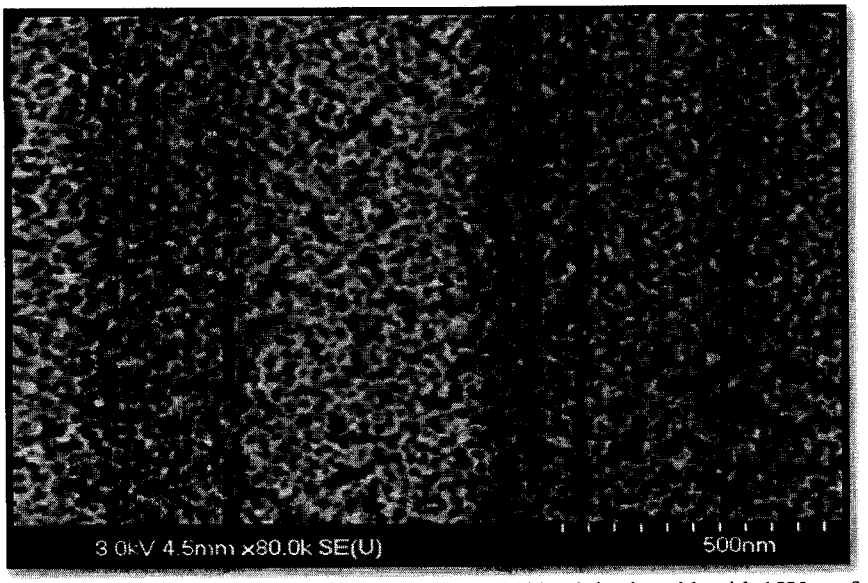

Figure 4.9. SEM micrograph of AAO template fabricated in 10% sulphuric acid, with $18V_{DC}$ after its first anodization step.

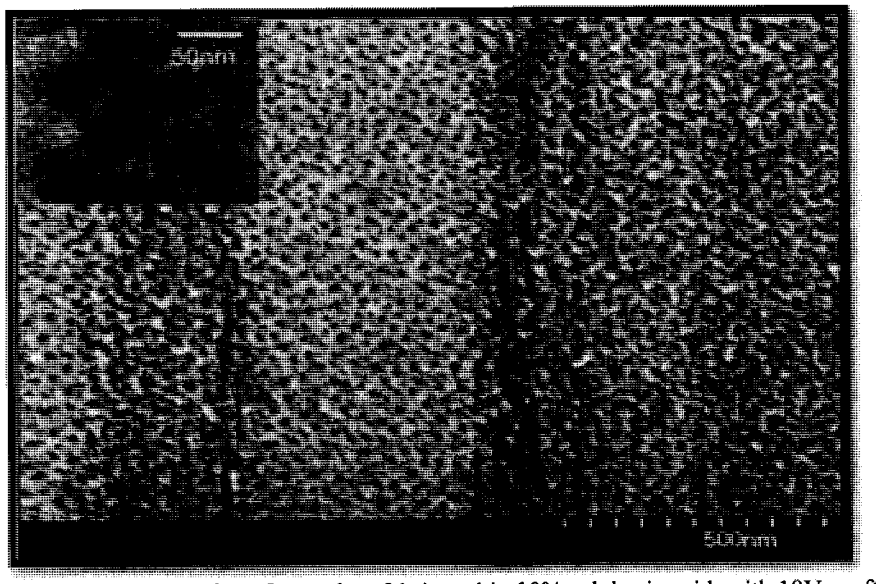

Figure 4.10. SEM micrograph of AAO template fabricated in 10% sulphuric acid, with $18V_{DC}$ after its second anodization step.

In Figure 4.10 it can be seen that pores are uniformly distributed and have interpore distance of 50nm. AAO templates were also fabricated in 0.3M oxalic acid, with ranging voltage of $35V_{DC}$ to $60V_{DC}$ with different anodization time and temperature to maximize the uniformity. With this electrolyte, the best result was obtained under $40V_{DC}$ at $4C^{o}$ which the SEM micrograph is illustrated in Figure 4.11.

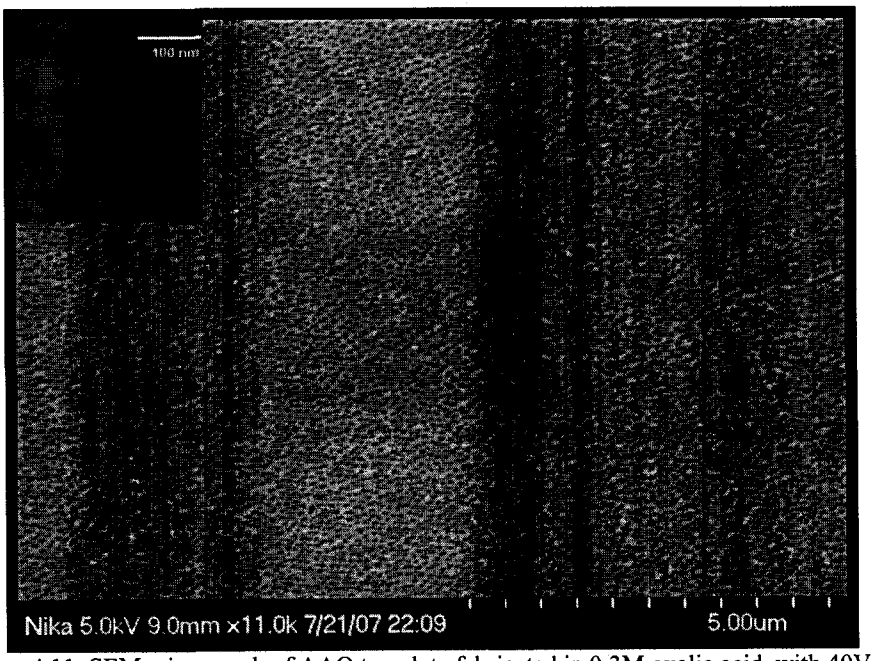

Figure 4.11. SEM micrograph of AAO template fabricated in 0.3M oxalic acid, with $40V_{DC}$.

The AAO template shown in Figure 4.11 has an average pore diameter of 40nm with 100nm interpore distance. It must be mentioned that there is a limited voltage range in which maximize the ordering of nanopores [4]. For instance Figure 4.12 shows a SEM micrograph of AAO fabricated in 10% sulphuric acid with the same condition as Figure 4.10 but with applied voltage of 32 V_{DC} . The pore diameter is ranging from 20 to 50 nm and there is no uniformity in the pore morphology.

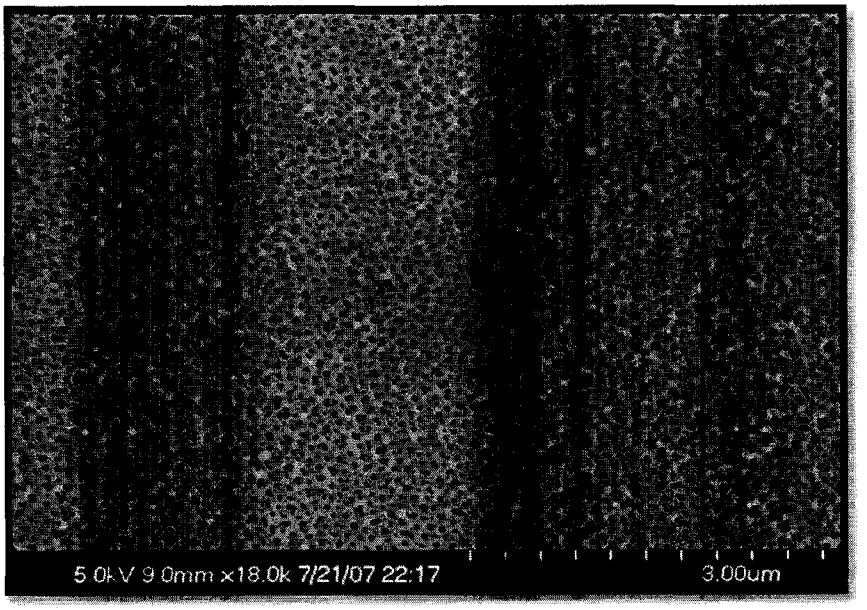

Figure 4.12. SEM micrograph of AAO template fabricated in 10% sulphuric acid, with $32V_{DC}$.

4.2.2. AFM study of AAO film

AAO templates fabricated by two step anodization were also studied by Atomic Force Microscopy (AFM) in its tapping mode. It is important to mention, to avoid imaging the electrolyte droplets sample surface, the samples were completely dried with nitrogen gun before imaging.

Figure 4.13 represent the AFM images of AAO template prepared by two step anodization of aluminum sheet in 10% sulphuric acid with 15 V_{DC} in 7C°.The aluminum substrate were removed with the same procedure that applied to the other samples. The image size is 2μm $\times 2\mu$m. As it can be seen in Figure 4.13 the AAO template has the pore diameter of 32nm and interpore distance of 40nm.

Figure 4.14 shows a magnified AFM image of the same template with 200nm × 200nm image size.

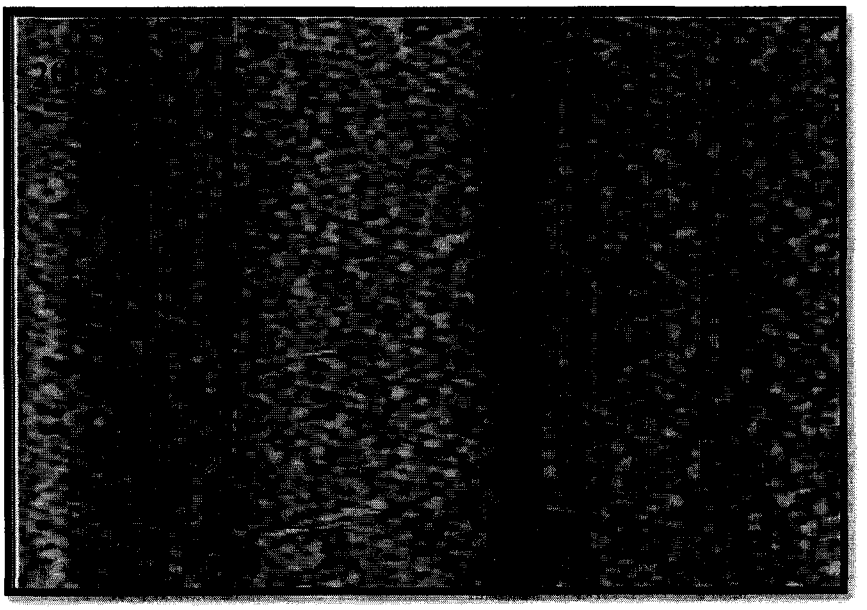

Figure 4.13. AFM image (2 μ m × 2 μ m) of AAO template fabricated with two step anodization, in sulphuric acid with $15V_{DC}$.

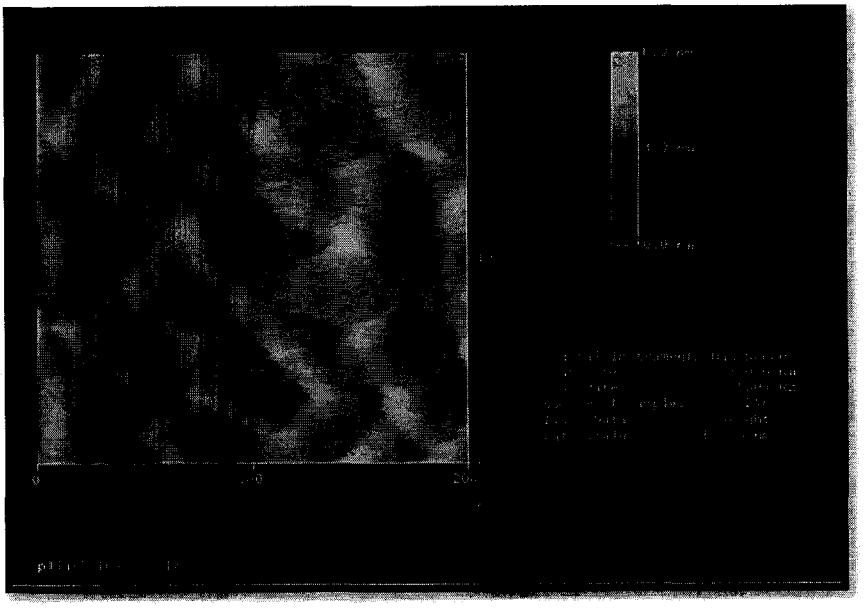

Figure 4.14. Magnified AFM image (200nm × 200nm) of AAO template fabricated with two step anodization, in sulphuric acid with $15V_{DC}$. Pore diameter of 32 nm and interpore distance of 40nm.

4.2.3. Variation of interpore distance with applied voltage

As it has been discussed in chapter 2, the interpore distance has a direct dependency on the applied voltage; therefore by increasing the voltage one can tailor the morphology of the AAO template.

Figure 4.15 depicts the interpore distance versus applied voltage of AAO template fabricated in oxalic and sulphuric acid that has been fabricated successfully in this research. The graph illustrates a linear relationship between the applied voltage and interpore distance that agrees with the work of others [21, 44].

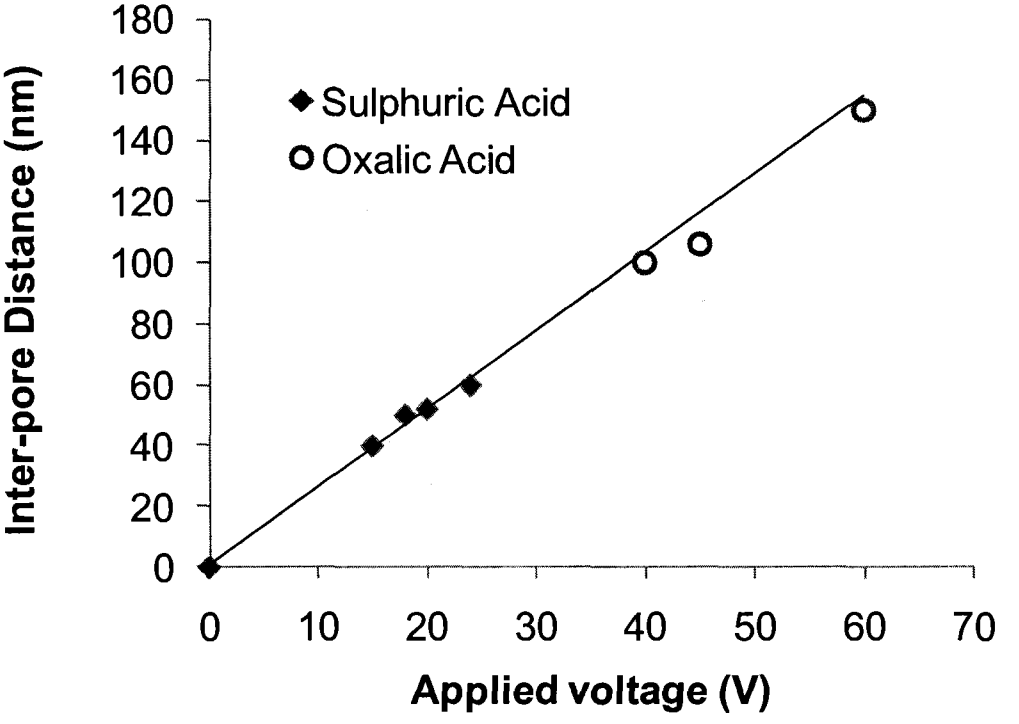

Figure 4.15. Interpore distance versus applied voltage of AAO template fabricated in sulphuric acid and oxalic acid.

4.3. Conclusion

Several AAO templates have been fabricated with different experimental parameters. The effects of anodization parameters on the morphology of these templates have been

studied. The main affecting parameters on the pore diameter and interpore distance are acidic environment and applied voltage. Interpore distance of AAO will increase linearly by increasing the voltage. Besides there are some specific range of voltages in each acidic medium that result in a well ordered pores. Templates with interpore distance of 40nm to 150nm were fabricated in 10% sulphuric acid and 0.3M oxalic acid.

Chapter 5: GIS fabrication, results and sensor application

5.1. Preparation of metallic nanowires

In this section the fabrication process of silver-gold alloy and silver nanowires by electrochemical deposition inside the pores of AAO will be described. As it has been discussed previously the electrochemical deposition of a metal within the pores of nanoporous membranes, entails the reduction of the desired metallic salt on the cathode. For this reason one side of the AAO template must be coated by a metal film to make the conductive contact of the cathode for electroplating. Therefore, to start the fabrication of nanowires the coating process of AAO template will be described in next section.

5.1.1. Coating the AAO with MagSput-2G2 sputtering machine

Sputtering is a process in which a thin film of desired material (target) will be deposited onto a sample inside a vacuum chamber. For this purpose, a high voltage will be applied across a low pressure gas such as Ar to form plasma consisting of high energy electron and ions. As the high energy ions hit the target that is connected to the cathode, the target atoms will be removed from its surface and deposited on the sample which located on the anode. Figure 5.1 illustrates a schematic view of vacuum chamber of a DC and RF sputtering machine.

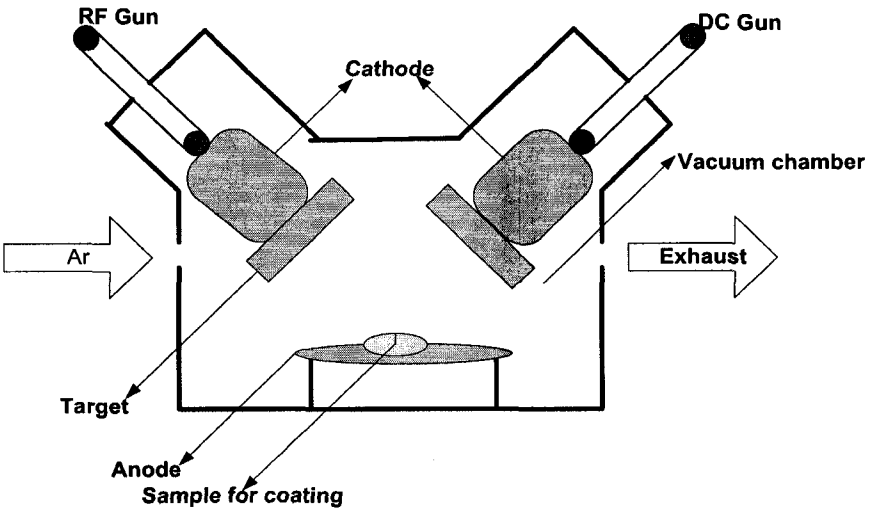

Figure 5.1. Schematic illustration of vacuum chamber of sputtering machine with DC and RF guns.

As it can be seen in Figure 5.1 there are two different guns exists for applying voltage. The DC gun is being used when the target is conductive and the RF gun is used for non-conductive targets.

The sputtering machine which was used in this research was Magnetron Sputtering system, model no: MagSput-2G2.

As it can be seen in above Figure there are 2 magnetron guns built in the sputtering machine chamber which have 5inch distance with the main substrate that the sample was fixed on it. The vacuum chamber is connected to a pumping system .The vacuum pumping system is a 150 l/s turbo molecular pump. A base vacuum of 10^{-6} can be achieved in about 45 minutes pumping.

To sputter gold, silver or titanium, we normally adjust the vacuum to 2×10^{-5} Torr. To get a good vacuum the chamber of the sputtering machine must be cleaned periodically by isopropyl alcohol. The system specification is shown in table 5.1.

Table 5.1. System specification of MagSput-2G2 sputtering machine.

Electrical power	120 V, 1 phase, 10 Amp
Cable	
Dry N_2 Gas	1/4 inch tube, 14psig swagelock fitting
Water	
Argon Gas	1/4 inch, 14 psig swagelock fitting

To coat one side of alumina template, the AAO will be mounted in a homemade made fixture where the fixture covers the holding ring and the other side of AAO was exposed to be coated via sputtering machine. The diameter of AAO film is 1.5 cm (A_{dep}= 1.77 cm^2). The fixture was placed inside the vacuum chamber and a noble metal such as gold or silver will be deposited on the AAO surface. The thickness of sputtered metal is 150-200 nm. The applied voltage, current flow and deposition rate of different metals that were used in this experiment is listed in the table.5.2.

Table.5.2. Applied voltage (V), current flow (A), sputtering rate (A°/s), and final thickness (nm) of different metals in MagSput-2G2.

Material	Plasma Voltage (Volt)	Current Flow (Ampere)	Sputtering Rate (A°/ s)	Final Thickness (nm)
Gold (Au)	650-700	85-90	28.3 A°/s	150-200
Silver (Ag)	500	80	21.1A°/s	150-200
Titanium (Ti)	800	230	0.1-0.4 A°/s	10

Figure 5.2 shows a photograph of MagSput-2G2 sputtering machine which was used in this experiment.

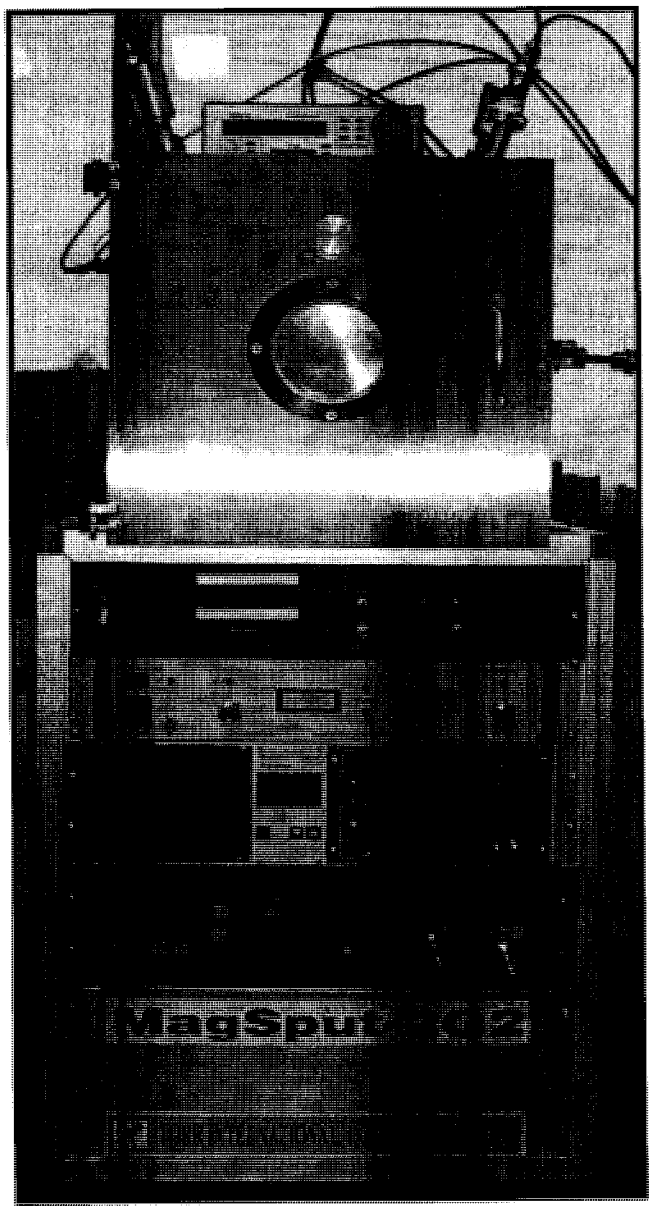

Figure 5.2. Photograph of MagSput-2G2 sputtering machine.

It must be mentioned that these values are highly dependent on the power output of any specific sputtering machine and the distance of the magnetic gun from the target.

After coating one side of alumina template with silver or gold, a metallic wire was connected to the sputtered side via conductive epoxy to make the required connection for electroplating. Figure 5.3 shows a photograph of sputtered alumina template with wire connection.

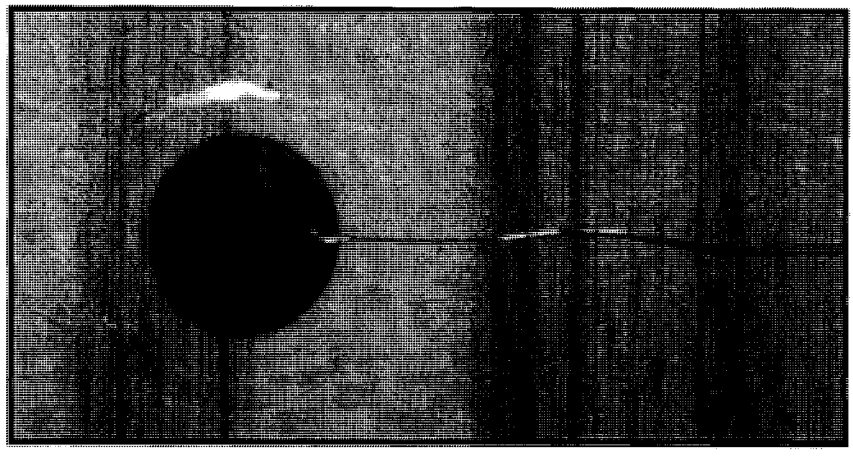

Figure 5.3. Photograph of alumina template coated with gold with wire connection.

5.1.2. Electrochemical deposition

Electrolyte is a solution which contains charged ions that comes from dissolution of a metallic salt in the water. When a sufficient amount of electric current passes through this electrolyte, the metal ions will be reduced into metallic solid in the working electrode. This process is referred to electroplating or electrochemical deposition [45].

In this experiment, the electrochemical deposition was carried out with three standard electrodes in the electrochemical cell. The working electrode is connected to AAO template, a noble metal (platinum) is connected to the auxiliary or counter electrode, and there is a reference electrode which includes saturated Ag/AgCl.

For this electrodeposition a galvanostatic transient method was applied in which the current between the working electrode and the counter (auxiliary) electrode, I, remained constant with a current source (galvanostat). The potential between the working electrode and reference electrode is recorded and plotted during the electrodeposition process.

Figure 5.4. illustrates a schematic diagram of electrochemical cell used in the galvanostatic measurement.

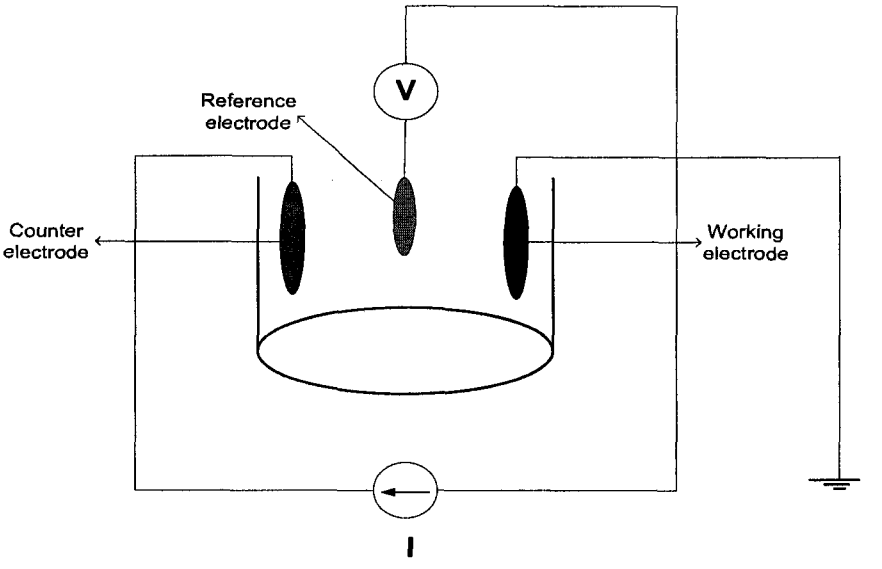

Figure 5.4. Schematic diagram of electrochemical cell used for galvanostatic measurement, where I is constant current source and V potential between reference electrode and working electrode that is recorded.

According to Helmholtz model [46], the changing arrangement of ions and electron will lead to the electrical double-layer charge at the interface of metal electrode and electrolyte solution. The electrical double-layer is related to a perfectly polarized layer, one on the metal (q_M) and the other in the electrolyte (q_S). This pair of charged layers will completely analogous to an electrical parallel-layer with a potential independent capacitance (C_{dl}).

Figure 5.5 illustrates the behaviour of response signal in an electrochemical cell by applying the input signal. The response signal is a function of time $V_i=f(t)$ in which shows that certain time is necessary to reach the potential V_i when the electrode reaction begins. If we consider this single-electrode reaction as a simplified equivalent RC circuit (Figure 5.5.B) the length of response time can be calculated [47].

When an invariable current applied to the electrodes, this current will be used for both charging the double-layer capacitance C_{dl} up to the require potential, and electron reaction (charge transfer).

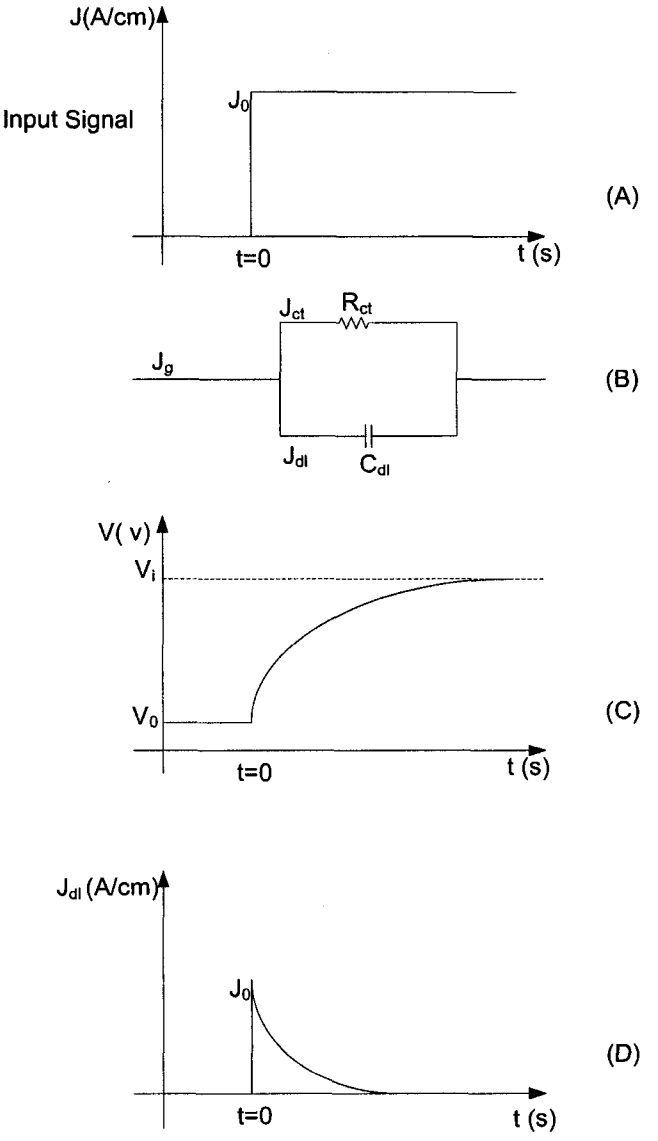

Figure 5.5. Behaviour of response signal in an electrochemical cell by applying the input signal, (A)Input signal(constant current)as applied to the template(working electrode), (B) Simplified equivalent circuit for single-electrode reaction, (C) Potential variation of working electrode versus time, (D) capacitive charging current versus time [45].

The total galvanostatic current density Jg can be shown as follow:

$$J_g = J_{dl} + J_{ct} \tag{5.1}$$

In which J_{dl} is the capacitive current and J_{ct} is the charge transfer (Faradic) current. After applying the current, the C_{dl} will be charged up to V_i in which the electrode reaction can start at a measurable rate. Figure 5.5.B shows the simplified equivalent RC circuit of the double-layer, therefore the instantaneous capacitive charging currant can be calculated as follow:

$$J_{dl} = J_0 \exp(-t/R_{ct}C_{dl}) \tag{5.2}$$

In which, J_0 is the input current density. Therefore the necessary time for C_{dl} to be charged up to its 99.0% of imposed voltage can be given as:

$$t_{v=0.99} = 4.6R_{ct}C_{dl} \tag{5.3}$$

This charging time is around few milliseconds. Figure 5.5.C shows the single-electrode reaction to the input signal, and the variation of potential of the working electrode, during the galvanostatic transient. Figure 5.5.D shows the capacitive charging current versus time [46, 48].

When the positive charged ions from the electrolytes accelerated toward the bottom of the pores, the ions will see the electrons which are supplied from the applied current and will be reduced into the metallic form. To calculate the quantity of deposited metal, the total cathodic charge (working electrode) can be calculated as follow:

$$Q = emnN_A \tag{5.4}$$

In which e represents the electron charge, m is number of gram moles of the deposited metal, n is number of electron taking part in the reduction, and N_A is the Avogadro constant which is 6.02×10^{23} mol^{-1}. If we consider F as the Faraday constant which is equal to $F = eN_A = 96435 Cmol^{-1}$.

The number of mole grams of the metal reduced by the Q charge can be given by:

$$m = Q/nF \tag{5.5}$$

In general, the total charge used in deposition can be calculated as the product of the current I (A) and the deposition time t_{dep}:

$$Q = \int_0^{t_{dep}} Idt \tag{5.6}$$

It is obvious if the electrodeposition done galvanostatically with constant I the above formula (5.6) can be transformed to $Q = I \times t_{dep}$. If we consider M_w as the atomic weight of the metal in grams, therefore, the weight of deposited metal, w, can be obtained as follow [2]:

$$w = mM_w = \frac{M_w}{nF} \int_0^{t_{dep}} Idt \tag{5.7}$$

Consequently, the thickness of the deposited material, T_{dep}, can be calculated by:

$$T_{dep} = \frac{w}{A_{dep} \times D_m} = \frac{mM_w}{A_{dep} \times D_m \times nF} \int_0^{dep} Idt \tag{5.8}$$

Where A_{dep} is the deposited area in cm, and D_m is the density of the metal in gram.cm^{-1}. If we know the porosity of the AAO template, P_{AAO}, the length of nanowires, L, can be easily estimated by:

$$L = T_{dep}/P_{AAO} \tag{5.9}$$

The theoretical calculation is only valid if we assume the deposition occur solely inside the pores of AAO template [49] . However, as the AAO template is suspended inside the electrolyte the deposition will occur, bilaterally on the both side of AAO template.

As, the alumina membrane which were fabricated in our lab had thickness around few microns, the handling of the AAO template with twisters was not easy to use for the further process of nanowires growing. Therefore in most of nanowire fabrication the commercial alumina template provided from Whatman Inc was used that are peripherally bonded to an annular polypropylene ring for easy handling. The commercial AAO known as Anopore (Anodisc), has two well-defined sides; the bottom side consist of pores with 20nm diameter and thickness of $2\,\mu$ and the bottom side consist of pores of 180nm with porosity of 109 per cm and thickness of $58\,\mu$.

Figure 5.6 shows a photograph of nanowires growing set up. The AAO template is suspended in glass beaker and connected to the working electrode, the platinum electrode is connected to the counter electrode, and the reference electrode including Ag/AgCl is suspended in the middle of beaker.

After preparing the set up, the electrodeposition will take place with galvanostatic current changing from 0.5 to 2 mA depending on the nature of electrolyte and the desired length of nanowires.

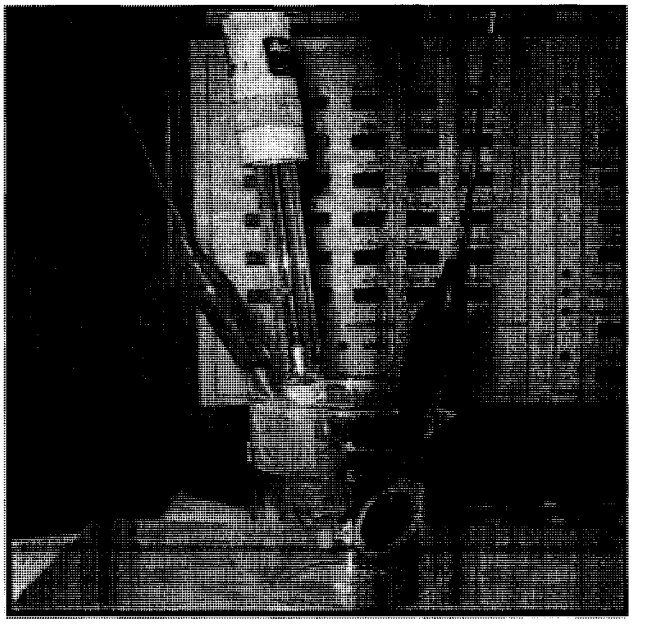

Figure 5.6. Photograph of nanowires growing set up, working electrode (AAO template)at right of beaker, counter electrode (platinum) at the left of beaker , and reference electrode is suspended in the middle of the beaker.

The solutions which were used in growing different metallic nanowires are as follow:

a) Orotemp 24T cyanide base gold to grow gold nanowires.

b) Ag_2SO_4 (0.4mM)$HAuBr_4$(1.3mM), $(NH_4)_2S_2O_3$(10mM) cyanide free solution to grow silver-gold alloy nanowires.

c) Silversene DW cyanide base silver solution to grow silver nanowires.

After a period of time, varying from 1 hour to 24 hours the AAO template were removed from the electrochemical cell and were cleaned with spacious of DI-water. The different electroplating time is for finding out the proper current and time to obtain well defined nanowires. Afterwards, the AAO templates were attached to a sputter coated silicon via diluted conductive paste. The sputter coated silicon contains 10nm titanium and 150nm gold or silver to provide an ohmic contact. It must be mentioned that the 10nm Ti work as an adhesive layer. After few hours that the diluted conductive paste dried, the AAO template was wash away by 1M NaOH from 10 minutes to 1 hour to obtain self standing metallic nanowires. Figure 5.7 illustrates a snapshot of silver nanowires which were grown inside AAO template and attached to sputtered coated silicon.

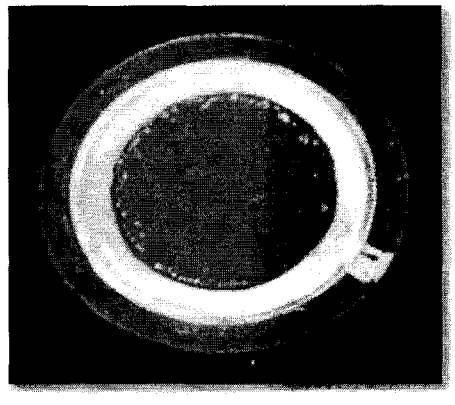

Figure 5.7. Photograph of silver nanowires inside AAO template and attached to sputtered coated silicon.

5.2. Result and discussion

In this section, results and discussion regarding the growth of nanowires, and their application as GIS will be presented.

5.2.1. Growth mechanism of nanowires

As it has been explained previously, the AAO template must be coated with a thin layer of gold or silver to act as a conductive contact for the working electrode. The electrodepositing area is an AAO template with 1.5cm diameter (A_{dep}= 1.77cm^2). To maximize the contact of electrolyte with the pores, the templates were fixed in the electrochemical cell in the way that the sputtered surface is faced the beaker and the open pores are exposed to the solution. As the electrodeposition of metal will take place bilaterally, both side of template will be covered by metallic films. Therefore, the backing metal film of AAO template will become thicker after a short period of time and will seal the back side of the pores completely [2].

The electrodeposition of metallic nanowires was carried out galvanostaticaly with a constant current.

To obtain the well ordered self-standing nanowires, electroplating with different current and time was tested. For the case of silver nanowires the best results were obtained with 2mA current for around 100 minutes.

To estimate the length of nanowires, we can go through the equations (Eqn.5.4 to Eqn.5.9). By applying the current value of 2mA for 100minutes, the total charge will be $Q = It = 2mA \times 6000 = 12C.$

The atomic weight and density of silver is M_{Ag}=108 gr, D_{Ag}=10.5gr/cm^3 respectively. Therefore, by substituting these value in relevant equations, the thickness of the deposited material, T_{dep}, will be 7.2 μm. The average porosity of AAO templates used in these experiments are 37.5%, consequently by refereeing to Eqn.5.9 the length of NWs (L) can be estimated as:7.2/0.375=19.2 μm. As the nanowire growth will happen

at the both side of the AAO template simultaneously, the estimated nanowire length is always longer than the actual ones.

Figure 5.8 shows the variation of working electrode potential (template) versus reference electrode (saturated Ag/AgCl), with time, during galvanostatic electrodeposition of silver nanowires for 100 minutes.

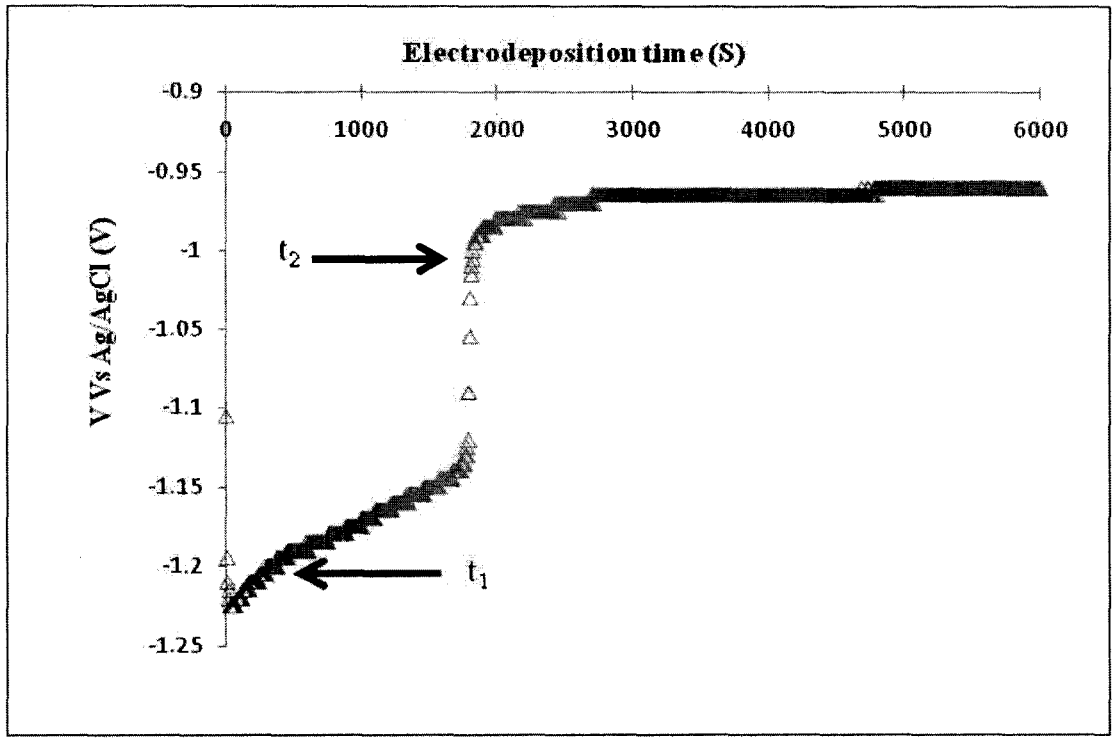

Figure 5.8. Potential variation of AAO template versus the reference electrode (Ag/Agcl).

As it is shown in above curve, the absolute value of the reaction potential V decreases with the time. This variation of potential can be explained as a result of change in concentration of Ag ions. As the number of Ag^+ increases near the AAO template (working electrode), the absolute value of v drops. After $t=t_2$, V remains constant during the electrodeposition as the pore will be filled out evenly.

5.2.2. SEM study of metallic nanowires

Figure 5.9 shows SEM micrograph of silver nanowires. As it has been explained previously the nanowires, start to grow in a tubular and after a period of time, the hollow tubular will be filled with the deposited metal resulting in a solid fibrils.

Figure 5.9. SEM micrograph of silver at its initiation stage of nanowire growth.

The electroplating of nanowires was carried out with different time to achieve the best result. At the beginning the silver-gold alloy nanowires were fabricated at room temperature for around 18 hours, with I=1mA. Figure 5.10 shows the SEM image of these nanowires. The substrate is tilted (45°) to expose the length of the nanowires. The silver-gold alloy nanowires are bundled together with average length of 20 μm.

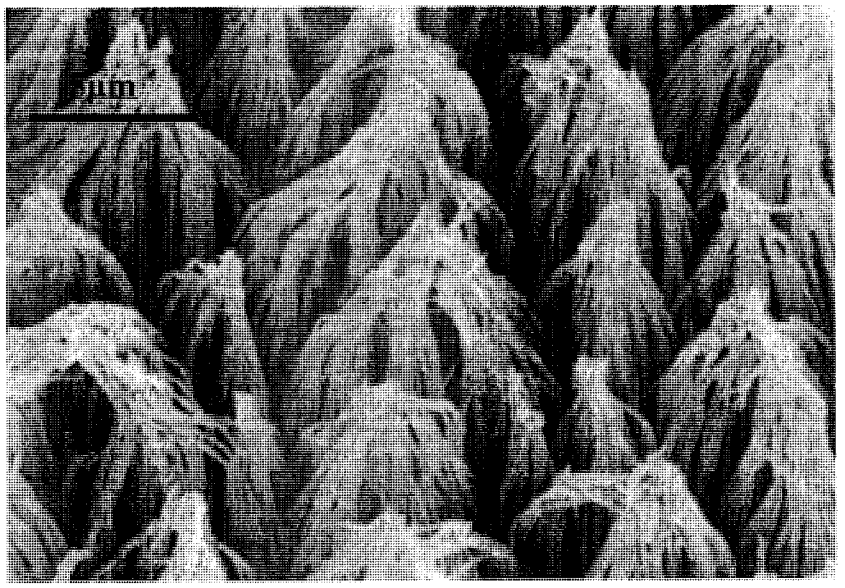

Figure 5.10. SEM micrograph of silver-gold alloy nanowire fabricated by 18 hours of electroplating.

The next experiment was carried out for the silver-gold alloy nanowire for 10 hours, with I=1mA. The SEM micrograph of cross section of these nanowires is shown in Figure 5.11.

Figure 5.11. SEM image of cross section of silver-gold alloy nanowires (electroplating in I=1mA and time=10 hours).

The length of nanowire is around 10μm, and less crumple can be seen in them comparing to the previous ones. Figure 5.12 shows the SEM micrograph of the same nanowire as above, in a top view image

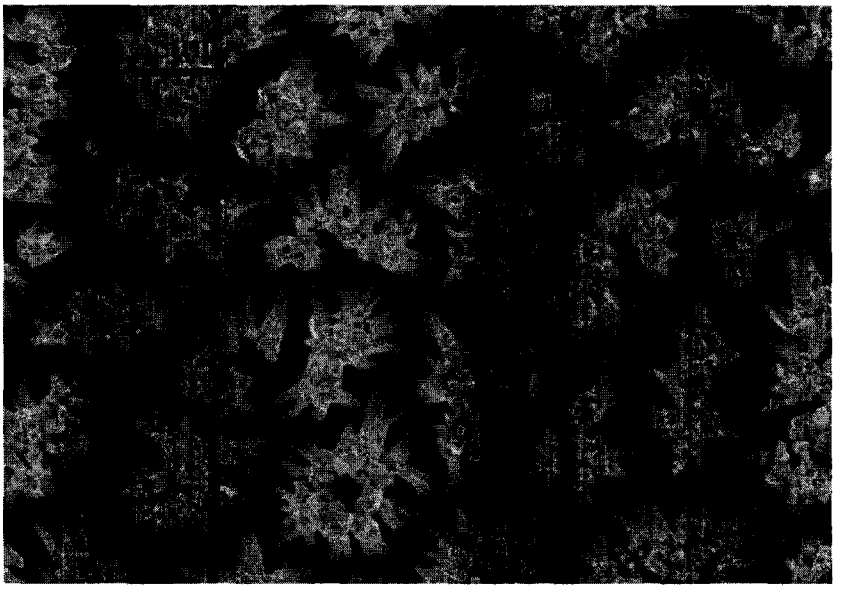

Figure 5.12. Top view SEM image of silver-gold alloy nanowires (electroplating in I=1mA and time=10 hours).

The tips of the wires are still attached together once their length increases more than few microns. To solve this problem, it is suggested to decrease the pore density [50] by immersing the AAO template into a suspension of polystyrene (PS) microspheres in water (0.05% w/v), before starting the nanowire growth. In this case, some random pores of the AAO template will be blocked and the density of pores will be decreased considerably.

Figure 5.13 illustrates silver-gold alloy nanowires, grown in the modified AAO template for 80 minutes with 2mA.

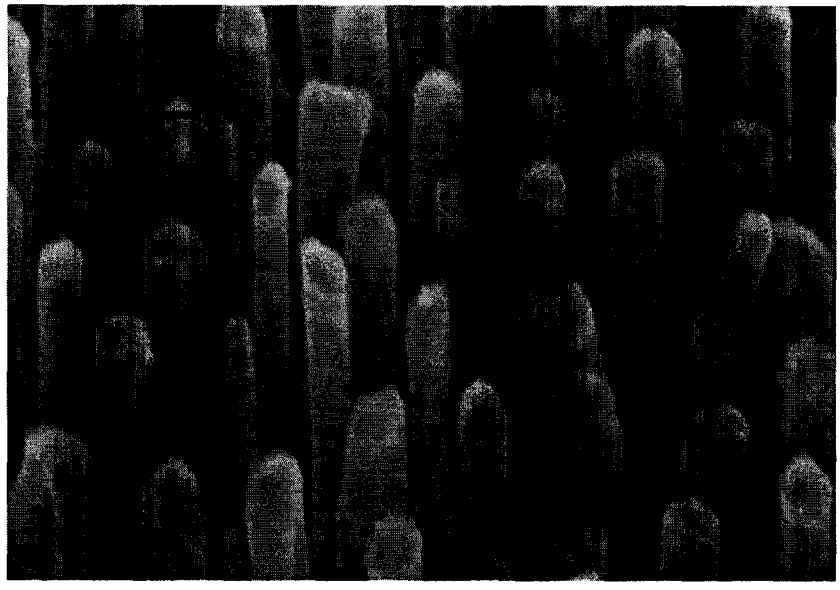

Figure 5.13. SEM micro-graph of silver-gold alloy nanowires, grown by 80 minutes electrodeposition with a constant current of 2mA.

As it is clear in the above image, the nanowires are self-standing and they didn't collapse on each other. The length of nanowires is about 4μm.

For the case of silver nanowires, the electrodeposition was held for 180 minutes with 1mA in the AAO template without any modification. Figure 5.14 shows SEM micrograph of these nanowires with 18μm length. As it is clear in the Figure 5.14 the same problem occurs, the nanowires bundle together after increasing their length more than few microns.

The same experiment was also carried out by modified AAO template with polystyrene (PS) microspheres for silver nanowires, for 100 minutes with constant current of 2mA. In this case, nanowires are almost self standing, and around 10μm long. Figure 5.15 shows the SEM image of these nanowires.

Figure 5.14. SEM micro-graph of silver- nanowires, grown by 180 minutes electrodeposition with a constant current of 1mA.

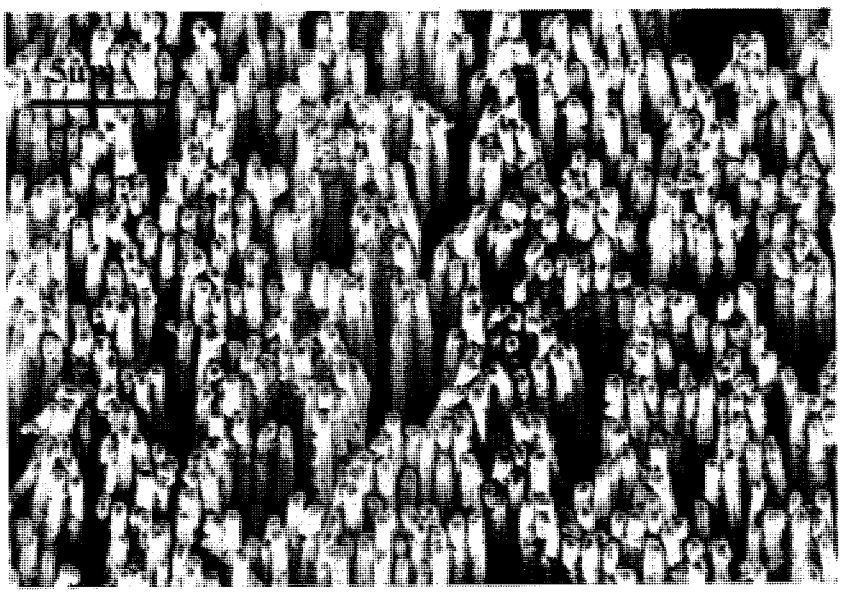

Figure 5.15. SEM micro-graph of silver nanowires, grown by 100 minutes electrodeposition with a constant current of 2mA

The self-sanding nanowires make it possible to utilize them as an electrode in the sensor application. The fabrication and operation of the GIS will be discussed thoroughly in the next section.

Figure 5.16 shows a comparison between silver-gold alloy and silver nanowire length versus the electroplating time. As it is clear the rate of silver deposition is a little bit faster than the silver-gold alloy.

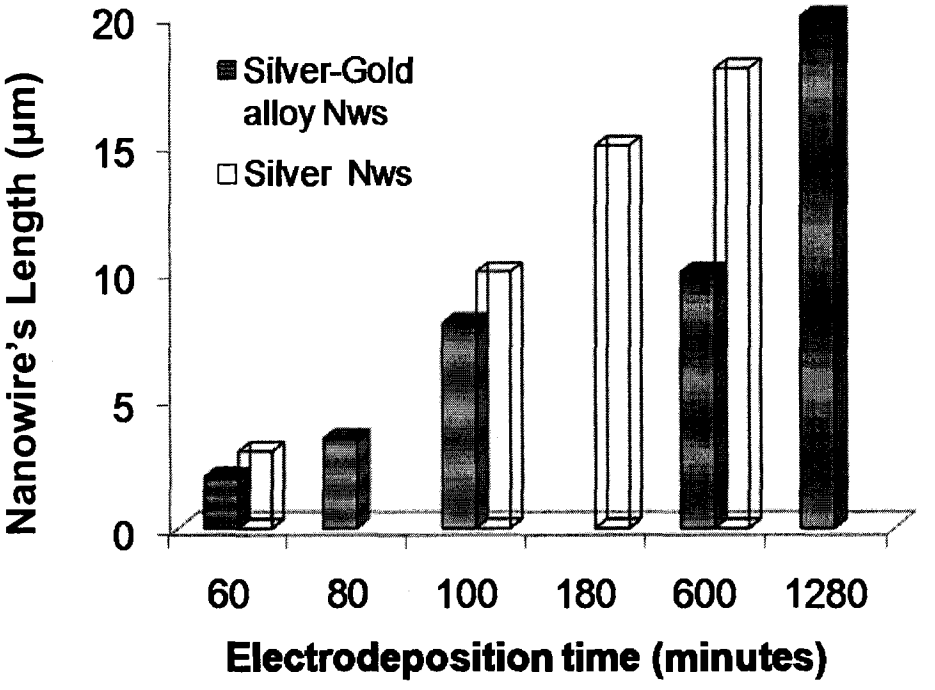

Figure 5.16. Silver-gold alloy and silver nanowire length (µm) versus electrodeposition time (minutes).

5.2.3. XRD study of silver-gold alloy nanowire

To confirm the existence of both silver and gold inside the silver-gold alloy nanowire, the XRD measurement was carried out for few samples. Figure 5.17 and Figure 5.18 shows the XRD of silver-gold alloy nanowire, in which the peaks for both silver and gold can be found in the graph.

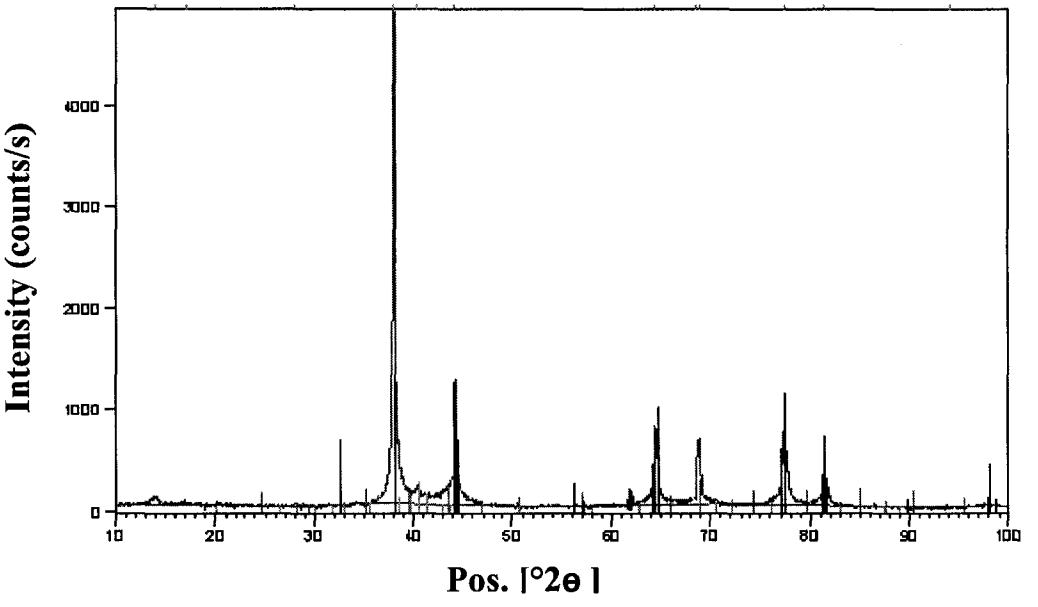

Figure 5.17. XRD pattern of silver-gold alloy nanowire.

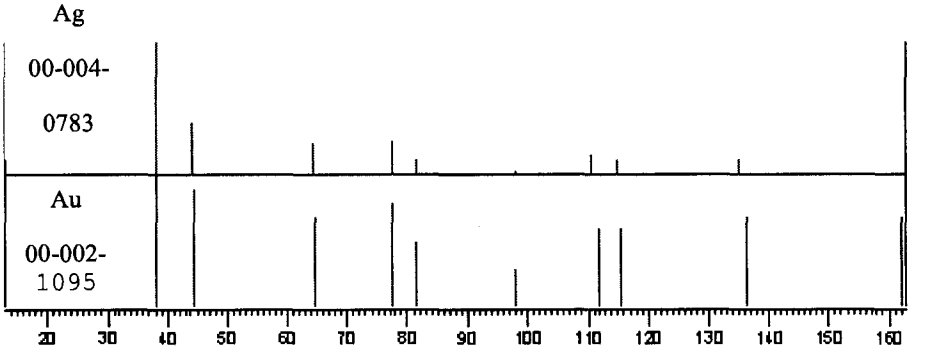

Figure 5.18. The XRD peak pattern of gold and silver in the silver-gold alloy nanowires.

5.3. Application of silver nanowires as the GIS

Sensors are critical devices in all measurement and controlling systems. These days the demand for sensors in all field of sciences, medicine, automated manufacturing and environmental monitoring is rapidly increasing. As the tiny and inexpensive sensors are finding their ways in all types of consumer product and industrial fields, sensor engineering is a multidisciplinary and interdisciplinary field of endeavour. In any controlling system there are many factors to be considered in choosing a proper sensor for that specific application.

The primary concern of choosing a sensor is the sensor characterization. The most important characteristics among them can be mentioned as sensivity, selectivity, stability and repeatability. It is obvious that a sensor is only useful if all these three parameters are exactly convinced [47].

Gaseous breakdown ionization sensors, will work by fingerprinting the ionization breakdown voltage of unknown gases. In the case of Gas Ionization Sensors (GISs), electron impact ionization mechanism will lead to the breakdown of gases and by measuring this voltage, existence of unknown gases can be found. The process of impact ionization entails of ionization by collision, in which a free electron collides with a neutral gas molecule and excite the molecule resulting a new electron and a positive ion [3]. Normally, the breakdown voltage of gases is in the range of several hundred to thousand volts which make it difficult or hazardous to employ in many environments [45].

Recently, breakdown ionization sensor has been reported using a film of aligned of carbon Nano tubes (CNT) arrays [51], and also self standing Au nanowires [52], at one electrode of parallel-plate. The applied electric field is amplified near the sharp tip of these ionization sensor, and due to formation of corona or conducting filament of highly ionized gas surrounding the tips, the breakdown process is hasten considerably [53].

5.3.1. Operation mechanism of GIS

In a two electrode configuration, there are always few electrons available which will be ionized by applying external electric field. The I–V characteristic of parallel electrode configuration has three main regions of gashouses discharge. The first region is known as quasi-ohmic region, in which the discharge current I, has a direct dependency on the applied voltage and is defined by the velocity of carriers. The second region is the saturation region, where I becomes independent of applied voltage as all the carriers generated in gap between the parallel plates has arrived at the electrode. At this stage the saturation current can be shown as follow:

$$I_{sat} = eAd\frac{dn_e}{dt} \tag{5.10}$$

Where e represents the electron charge, A is the electrode area, d is the gap between the parallel electrodes and dn_e/dt is the rate of radiation-induced electron production in d spacing [47]. As the voltage increases gradually, gas ionization in between of electrodes will occur by electron impact and will give rise to I at an increasing rate till the gas breakdown happens at V_b. Therefore the characteristic between the saturation region and breakdown voltage represent the third pre-breakdown region which refers to Townsend's discharge and the current can be shown as:

$$I = \frac{I_{sat} \times e^{\alpha d}}{1-\gamma(e^{\alpha d}-1)} \tag{5.11}$$

Where, α and γ are Townsend's primary and secondary ionization coefficients. α shows the number of ionizing collisions an electron made by accelerating for 1 cm in the field direction and γ represents the number of electrons which liberated per incident ion at the cathode [47]. As, α and γ are the functions of the electric field, so V_b is known as the point in which could affect them in a manner that the denominator of Eqn.5.11

becomes zero. Consequently, the current would will rise dramatically at V_b and become self-sustained [52].

According to the Paschen's law the breakdown voltage of the gases in a two parallel plates, is directly dependant on the concentration of the gas N, and the gap distance d [47].

$$V_b = f(Nd) \tag{5.12}$$

By considering the general rule of gases, pressure of the gases P is proportional to N at a constant temperature. Therefore, the sensivity of the GIS can be based on V_b-P, and as a very sensitive device it is expected to work with gases at very low pressure.
The main advantage of using self-standing nanowires in synthesizing of GIS, is that the high aspect-ratio of nanowires on the surface of electrode will provide locally enhanced electric field at the top of the nanowires tip where:

$$E_{loc} = \beta E_{app} \tag{5.13}$$

In which E_{app} is the applied electric voltage defined as V/d in two parallel plate sensor, and β is the field enhanced factor that is dependent on the device geometry and will increase by elongating nanowires aspect-ratio and tip sharpness [47].
It is important to note that, it is assumed that the scale of total nanowires length is much smaller than the d spacing gap between the parallel plates of the GIS.

5.3.2. Fabrication Process of GIS

As it has been discussed previously, the fundamental architecture of the GIS is made of two parallel plates (electrodes) of metal, in which the gas ionization occur. For this purpose, one electrode is made of self-standing silver nanowires film attached to its companion substrate which is exactly the same way that has been discussed previously. For a secondary electrode a double side polished p-type silicon wafer was used. In order to provide an ohmic junction in the p-type silicon, the wafer is coated with 1μm layer of

aluminum on its both sides and then it has been annealed in a N_2+H_2 ambient at 400°C for 40 minutes.

To make the d spacing between the two electrodes, a supporting polypropylene ring was attached to the AAO template, while engraving four tiny grooves around the ring to assist the venting flow in between of the parallel plates. Polypropylene is recognized as a material with high electrical strength or high volume resistivity [45].

Figure 5.19 illustrates a schematic view of GIS made of a plate of nanowires film and an Al coated silicon wafer as the counter electrode.

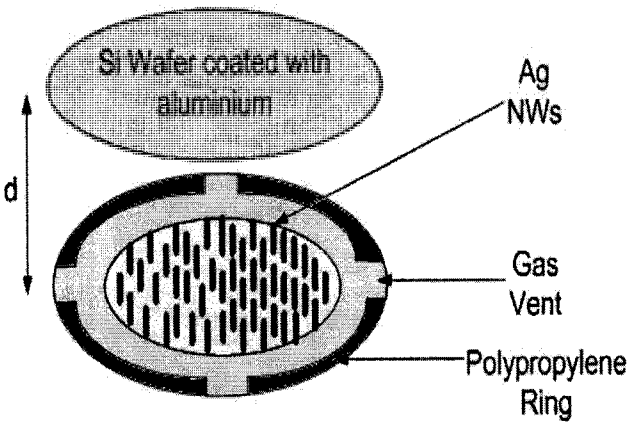

Figure 5.19. Schematic diagram of the GIS.

To make an ohmic contact on the each electrode a metallic wire was connected via silver epoxy on their surfaces. To examine the sensor with different gaseous medium, the GIS was placed inside the vacuum chamber and the air inside the chamber was pumped down to 10^{-6} Torr. The two electrodes were connected individually to two source-measure units (SMU) in which the electrode currents can be measured separately. Two SMU channels of HP4155 semiconductor parameter analyzer was used to characterize the GIS [53].

5.3.3. Results and discussion regarding GIS operation

5.3.3.1. Pre-Breakdown measurements

To measure the pre-breakdown discharge current (I) of the GIS at very low pressure (10^{-6} Torr) with a sweep voltage up to ±200V (Δt = 1s, ΔV = 1V) was used. Fig.5.20 illustrates the I-V curve of the anode and cathode of the GIS under 10^{-6} gas pressure, while the AgNWs film is used as the cathode. It is clear that, I (anode) is remarkably higher when the AgNWs are used as the cathode because of the enhanced ionization of low pressure gas caused by repulsion of electrons.

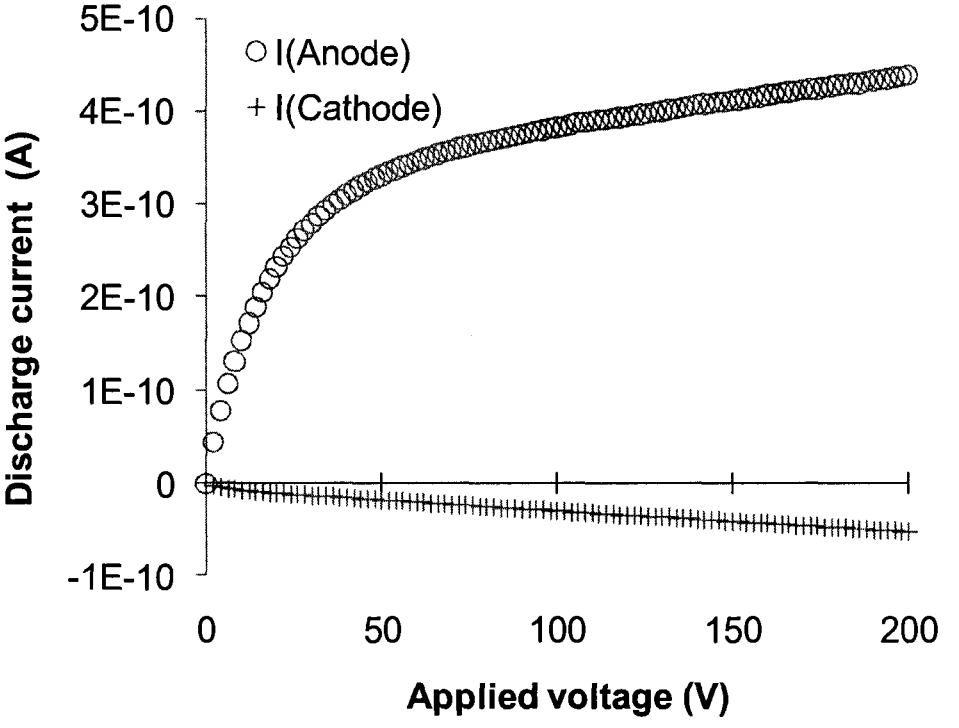

Figure 5.20. Pre-breakdown discharge current of both electrodes of the GIS with silver nanowires, in low pressure air (P = 10^{-6} Torr, T = 22°C), for AgNWs film as the cathode.

As it can be seen in Fig.5.20, the anodic current starts to increase by, augmenting the applied voltage, and after passing the quasi-ohmic region, it reaches the saturation region similar to a uniform field in a parallel plates, where there is no impact ionization in the d spacing between the two electrodes. At this stage the current remains

voltage-independent up to the point where the Townsend discharge starts at the higher voltage.

Since the pressure is kept constant during the sweep, the slight increase in I_{sat} can be solely attributed to abnormal electron repulsion from the AgNWs tips [52]. These electrons can trigger secondary ionizations in the gap at very low gas pressures, therefore, increases dn/dt (Eqn.5.10).

5.3.3.2. Breakdown Voltage in the GIS

The breakdown voltage of ultra-pure argon was measured at the pressures in the range of $10^{-4} < P < 10^{-1}$ torr, at room temperature.

The I–V curves of ultra-pure argon taken at different gas pressures are shown in Figure 5.21. It is clear that V_b decreases by increasing P, which indicates that the tested gas pressures were less than the Paschen minimum. Above 0.1 torr, V_b is expected to remain unchanged [45].

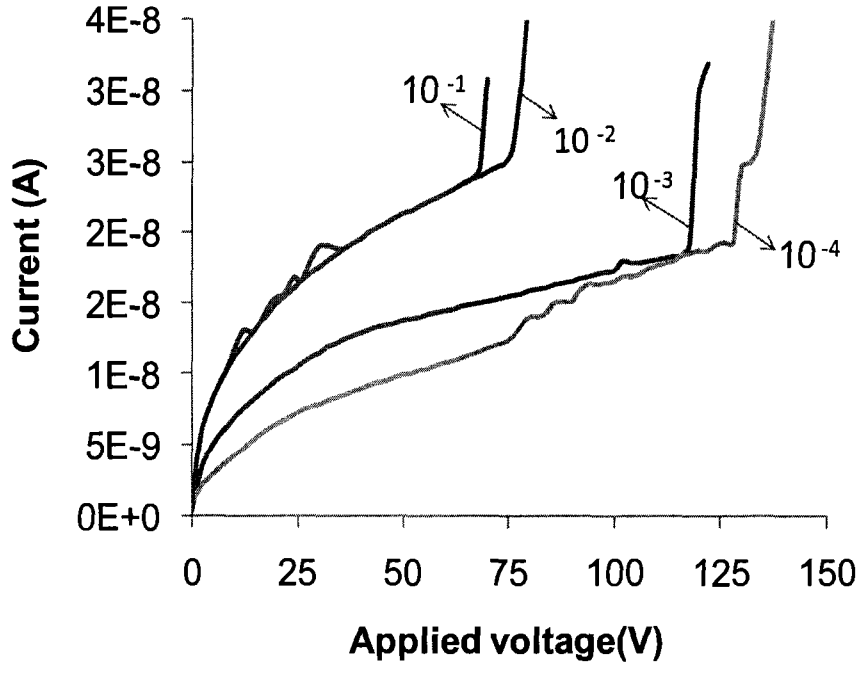

Figure 5.21. The *I–V* curves obtained in argon ($10^{-4} \leq P \leq 0.1$ torr).The relevant pressure is shown on each of the curves.

Comparing the value of V_b in these devices with two parallel-plate structures, the V_b is significantly reduced, considering the same spacing and gas pressure. As it was explained in the theoretical section, the sharp tip of the nanowires enhances the local electric field (E_{loc}) at the tips by a factor of β, and will provoke ionization of the gas molecules at a lower E_{app}. Table.5.3 represents a comparison between Ar gas breakdown voltage between GIS fabricated with AuNWs and AgNWs, with the same sensor structure and gas pressure. As it can be seen, V_b in AgNW-GIS is considerably decreased, especially in the left side of the Paschen's curve.

Table 5.3. Comparison of breakdown voltages of Ar in the GIS, fabricated with both AuNws and AgNws.

Ar gas pressure (torr)	10^{-4}	10^{-3}	10^{-2}	10^{-1}
V_b in AgNWs as cathode (V)	128	118	76	68
V_b in AuNWs as cathode (V)	>400	>400	187	163

5.4. Conclusion

Silver and silver-gold alloy nanowires have been fabricated with electrodeposition of their metallic salt inside the AAO template. The free standing metallic nanowires were obtained with different aspect ratio.

The application of these nanowires was in the fabrication of the GIS. The GIS was tested in low pressure argon gas ($0.1 \leq P \leq 10^{-4}$ torr) where the breakdown voltages (V_b) were recorded against pressure. This GIS showed improvement compared to its previous AuNWs counterpart, as the breakdown voltages were further reduced. The reduction of V_b was attributed to the lower workfunction of silver compared to that of gold.

Chapter 6: Conclusions, contributions and future works

6.1. Conclusions and contributions

In this work, we fabricated the nanoscale elements of the miniaturized Gas Ionization Sensor based on the metallic nanowires, and also GIS based on arrays of AgNWs. The GIS operates by measuring the breakdown voltages of the unknown gases in a very low gas pressure.

To obtain the GIS with high sensivity first we had to obtain well ordered metallic nanowires with desired aspect ratio, therefore, the AAO template for electroplating was fabricated. The AAO templates were fabricated using the modified two steps anodization process. Different samples have been prepared with various anodization conditions to obtain well-ordered templates. Besides, it has been demonstrated that interpore distance of the AAO is directly proportional to the applied voltage which make it possible to fabricate tailored AAO templates. Templates with interpore distance of 40 nm to 150 nm were fabricated in 10% sulphuric acid and 0.3M oxalic acid.

The freestanding arrays of metallic nanowires were synthesized in the pores of AAO template. These arrays of metallic nanowires were incorporated as the field amplifier element to decrease the breakdown voltages of the gases in the GIS.

To optimize the operation of the GIS, silver-gold alloy and silver nanowires with different aspect ratio was fabricated. The best result was achieved with the 10 μm silver nanowires, where the non-uniform electric fields at the tip of the nanowires hastened the breakdown voltage of the gases and made it possible for the GIS to identify the unknown gases in the very low ($0.1 \leq P \leq 10^{-4}$ torr) gas pressure.

The new device displayed considerably lower V_b compared to its gold nanowire (AuNW)-based counterparts. The reduction of V_b was justified based on the increase in

the secondary electron emission factor on AgNWs due to the lower workfunction of silver.

The contributions of this research are summarized as follow:

- Anodized Aluminium Oxide (AAO) template was fabricated with different interpore distance varying from 40 nm to 150 nm.
- The dependency of the AAO morphology on the anodization condition was studied.
- Freestanding silver-gold alloy and silver nanowires with different aspect ratios were synthesized. To avoid bundling of the nanowires the porosity of the AAO was reduced, using polystyrene microsphere as the pore blockage.
- Gas ionization sensor based on the AgNWs arrays at the cathode of a two parallel-plate of ionization cell was fabricated.
- The fabricate GIS was successfully tested for Ar gas in a very low gas pressure.
- The AgNWs-based GIS was compared to its AuNWs –based counterpart.

6.2. Future works

The concept of gas ionization sensor based on arrays of self-standing nanowire for fingerprint the breakdown voltages of unknown gases can be developed further. As the AAO template is the basic elements of the nanowire fabrication in this GIS, it is worth to improve the new techniques to have inclusive control over its morphology and pattern. Therefore, it is expected to obtain more sensitive and complicated device by using modern nano patterning techniques in fabrication GIS elements.

- GIS based on the metallic nanowires with uniform distribution can be tested.
- The complete uniform distribution can be obtained by fabricating ideal AAO template with homogeneous pore diameter and interpore distance via modern lithographic methods.

- Study the breakdown and ionization of different gases with AgNWs GIS.
- Study the breakdown and ionization of the GIS for gas mixture.
- Fabrication of the GIS base on other noble metals to achieve lower breakdown voltage.

References

[1] R. B. Sadeghian, and M. Kahrizi, "A novel miniature gas ionization sensor based on freestanding gold nanowires," *Sensors and Actuators A: Physical,* vol. 137, pp. 248-255, 2007.

[2] R. B. Sadeghian, "A field effect gas sensor based on self-standing nanowires arrays," *A PhD Thesis in Department of Electrical and Computer Engineering,* Concordia University, 2007.

[3] R. B. Sadeghian, and M. Kahrizi, "A low voltage gas ionization sensor based on sparse gold nanorods," in *IEEE Sensors Conf.*, Atlanta, GA, 2007, pp. 648-651.

[4] N. Azmoodeh, R. B. Sadeghian, and M. Kahrizi, "Study of the effect of anodization parameters on the morphology of anodic aluminium oxide films," 2007, *the thirteen Canadian Semiconductor Technology Conference,* Aug 14-17, 2007, Montreal, Canada

[5] C. Z. Li, A. Bogozi, W. Huang, and N. J Tao, "Fabrication of stable metallic nanowires with quantized conductance," *Nanotechnology* vol. 10, p. 4, 1999.

[6] Y. Xia, P, Yang, Y. Sun, Y. Wu, B. Mayers, B. Gates, Y. Yin, F. Kim, and H. Yan, "One-dimensional nanostructures: synthesis, characterization, and applications," *Advanced Materials,* vol. 15, pp. 353-389, 2003.

[7] K. Sivakumar, "Nanowire sensor and actuator." *A Master thesis in department of electrical Engineering, University of Delaware, Delaware,* 2006.

[8] V. Rodrigues, and D. Ugarte, "Metal nanowires: atomic arrangement and electrical transport properties " *Nanotechnology,* vol. 13, p. 5, 2002.

[9] R. Könenkamp, R. C. Word, and C. Schlegel, "Vertical nanowire light-emitting diode," *Applied Physics Letters,* vol. 85, p. 3, 2004.

[10] Z. Q. Liu, W. Y. Zhou, L. F. Sun, D. S. Tang, X. P. Zou, Y. B. Li, C. Y. Wang, G. Wang, S. S. Xie, "Growth of amorphous silicon nanowires," *Chemical Physics Letters,* vol. 341, p. 6, 2001.

[11] http://www.nsti.org/Nanotech2008/symposia/Nano_Fabrication.html#TH22.1, 7 March 2008

[12] L. Uzi, R. N. Barnett, and W. D. Luedtke, "Nanowires: size evolution, reversibility, and one-atom contacts," *Zeitschrift für Physik D Atoms, Molecules and Clusters,* vol. 40, pp. 282-287, 1997.

[13] A. Huczko,"Template-based synthesis of nanomaterials", *Applied Physics A: Materials Science & Processing,* vol. 70, p. 12, 2000.

[14] J. C. Hulteen, and C. R. Martin, "A general template-based method for the preparation of nanomaterials," *Journal of materials chemistry,* vol. 7, p. 13, 1997.

[15] G. Riveros, S. Green, A. Cortes, H. Gomez, R. E Marotti, and E. A. Dalchiele, "Silver nanowire arrays electrochemically grown into nanoporous anodic alumina templates," *Nanotechnology,* vol. 17, p. 10, 2006.

[16] C. Ji, "Synthesis, characterization and applications for gold-silver alloy and nanoporous gold nanowires," *Ph.D. dissertation, Johns Hopkins University, United States, Maryland,* 2003.

[17] V. P. Menon and C. R. Martin, "Fabrication and evaluation of nanoelectrode ensembles," *Anaytical Cheistry.,* vol. 67, pp. 1920-1928, 1995.

[18] M. Tian, J. Wang, J. Kurtz, T. E. Mallouk, and M. H. W. Chan, "Electrochemical growth of Single-Crystal Metal Nanowires via a Two-Dimensional Nucleation and Growth Mechanism," *Nano Letter,* vol. 3, pp. 919-923, 2003.

[19] J. P. O'Sullivan, G. C. Wood, "The Morphology and Mechanism of Formation of Porous Anodic Films on Aluminium," *Proceedings of the Royal Society of London. Series A, Mathematical and Physical Sciences* vol. 317, pp. 511-543, 1970.

[20] G. E. Thompson, "Porous anodic alumina: fabrication, characterization and applications," *Thin Solid Films,* vol. 297, pp. 192-201, 1997.

[21] P. Larson, "Fabrication and characterization of ordered arrays of nanostructures,". *Ph.D. dissertation, University of Oklahoma, United States, Oklahoma.* , 2005.

[22] Y. Li, Y. Kanamori, and K. Hane, "A new method for fabrication nano-porous aluminum grating array," *Microsystem Technologies,* vol. 10, pp. 272-274, 2004.

[23] O. Jessensky, F. Muller, and U. Gosele, "Self-organized formation of hexagonal pore arrays in anodic alumina," *Applied Physics Letters,* vol. 72, pp. 1173-1175, 1998.

[24] K. Nielsch, J. Choi, K. Schwirn, R. B. Wehrspohn, and U. Gosele, "Self-ordering Regimes of Porous Alumina: The 10% Porosity Rule," *Nano Letter.,* vol. 2, pp. 677-680, 2002.

[25] M. Wirtz, C. R. Martins,"Template-fabricated gold nanowires and nanotubes," *Advanced Materials,* vol. 15, pp. 455-458, 2003.

[26] G. Che, B. B. Lakshmi, C. R. Martin, E. R. Fisher, and R. S. Ruoff, "Chemical vapor deposition based synthesis of carbon nanotubes and nanofibers Using a template method," *Chemical Materials,* vol. 10, pp. 260-267, 1998.

[27] M. Sun, "Fabrication and characterization of ultra-uniform magnetic nanoparticle arrays in ordered aluminum oxide templates," *Ph.D. dissertation, The University of Alabama, Alabama,* 2001.

[28] W. Xin, and H. Gao-Rong, "Fabrication and characterization of anodic aluminum oxide template," *Microelectronic Engineering,* vol. 66, pp. 166-170, 2003.

[29] H. Y. H. Masuda, M. Satoh, and H. Asoh, "Highly ordered nanochannel-array architecture in anodic alumina," *Applied Physics Letters,* vol. 71, p. 3, 1997.

[30] J. W. Diggle, T. C. Downie, and C. W. Goulding, "Anodic oxide films on aluminum," *Chem. Rev.* , vol. 69, p. 11, 1968.

[31] Y. Sui and J. M. Saniger, "Characterization of anodic porous alumina by AFM," *Materials Letters,* vol. 48, pp. 127-136, 2001.

[32] http://en.wikipedia.org/wiki/Atomic_force_microscope, 19 March 2008.

[33] http://spm.phy.bris.ac.uk/techniques/AFM/, 6 April l2008.

[34] "Scaning Probe microscopy Training notebook," *digital instruments Veeco Metrology Group,* version 3.0, 2001.

[35] A. Author Brenner, "Electrodeposition of alloys: principles and practice," *New York, Academic Press, 1963,* vol. 2, 1963.

[36] M. Ohring, "Materials Science of Thin Films," *Academic press, 2nd Edition,* 2002.

[37] "http://www.uccs.edu/~tchriste/courses/PHYS549/549lectures/image.html,"9 May 2008.

[38] "http://www.mse.iastate.edu/microscopy/path.html,"9 May 2008.

[39] S. Manual, "Hitachi S-4700 SEM Training & Reference Guide" 2007.

[40] "http://www.panalytical.com/index.cfm?pid=135," 11 May 2008.

[41] "http://en.wikipedia.org/wiki/Bragg's_law," 12 May 2008.

[42] "http://en.wikipedia.org/wiki/Electropolishing," 12 May 2008.

[43] S. Zhao, K. Chan, A. Yelon, T. Veres, " Preparation of open-through anodized aluminium oxide films with a clean method," *Nanotechnology,* vol. 18, p. 5, 2007

[44] M. Tian, S. Xu, J. Wang, N. Kumar, E. Wertz, Q. Li, P. M. Campbell, M. H. W. Chan, and T. E. Mallouk, "Penetrating the oxide barrier in situ and separating freestanding porous anodic alumina films in one step," *Nano Letter,* vol. 5, pp. 697-703, 2005.

[45] A. P. Li, A. Birner, K. Nielsch, and U. Gösele, "Hexagonal pore arrays with a 50-420 nm interpore distance formed by self-organization in anodic alumina", *Journal of applied physics,* vol. 84, 1998.

[46] R. Banan-Sadeghian and M. Kahrizi, "A Novel Gas Sensor Based on Tunneling-Field-Ionization on Whisker-Covered Gold Nanowires," IEEE Sensors Journal, 2007.

[47] "http://en.wikipedia.org/wiki/Double_layer_(interfacial)," 23 May 2008.

[48] A. M. Howatson, "*An introduction to gas discharges*", 2nd ed. Oxford: Pergamon Press, 1976.

[49] A. Knoblauch, C. Wilbertz, T. Miller, and S. Kalbitzer, "Field electron emission properties of a supertip," *Journal of Physics D: Applied Physics*, vol. 29, pp. 470-473, 1996.

[50] M. S. a. M. Paunovic, "Modern Electroplating," *Wiley, New York,* vol. 4th edition, 2000.

[51] R. B. Sadeghian, "Ultra-low voltage schottky barrier field enhanced electron emission from gold nanowires electrochemically grown in modified porous alumina templates," *IEEE Electron Device Letters,* 2007.

[52] A. Modi, N. Koratkar, E. Lass, B. Wei, and P. M. Ajayan, "Miniaturized gas ionization sensors using carbon nanotubes," *Nature,* vol. 424, pp. 171-174, 2003.

[53] R. B. Sadeghian and M. Kahrizi, "A Low Pressure Gas Ionization Sensor Using Freestanding Gold Nanowires," in *IEEE ISIE*, Vigo, Spain, 2007, pp. 1387-1390.

[54] N. Azmoodeh, R. B. Sadeghian, and M. Kahrizi, "A silver nanowire based gas ionization sensor," *Biodevice,* Jan 14-17 2009, submitted